E3 Ubiquitin Ligase Highwire/Phr1 Phase Separation Mediates Endocytic Control of JNK Signaling in *Drosophila* Neurons

Srikanth Pippadpally[1*], Anjali Bisht[1], Saumitra Dey Choudhury[1,3#], Manish Kumar Dwivedi[1#], Zeeshan Mushtaq[1#], Suneel Reddy-Alla[2] and Vimlesh Kumar[1*]

[1] Department of Biological Sciences, Indian Institute of Science Education and Research (IISER) Bhopal, Academic Building 3, Bhauri, Bhopal-462 066, Madhya Pradesh, India.

[2] College of Community Science, Acharya N.G. Ranga Agricultural University, Guntur-522034, Andhra Pradesh, India

[3] Present Address: Centralized Core Research Facility (Microscopy) Convergence Block, All India Institute of Medical Sciences (AIIMS), Ansari Nagar, New Delhi- 110029, India

# Equal contribution

* Author for correspondence

Corresponding author: Phone - +91 755 2691405

Fax - +91 755 2692392

Email- psrikanth20@iiserb.ac.in; vimlesh@iiserb.ac.in

Running title: Endocytosis restricts synaptic growth via phase-separated Hiw/Phr1

Keywords: Endocytosis; BMP pathway; JNK pathway; Highwire condensates; Wallenda; Rab11; Synaptic growth signaling

Abstract

Synaptic growth and organization are orchestrated by pre- and post-synaptic signaling, neuronal activity, and environmental cues. Although endocytosis is known to attenuate synaptic growth, the underlying signaling mechanisms have remained elusive. Here, we uncover a previously unrecognized mechanism by which endocytosis constrains synaptic growth through regulation of the neuronal E3 ubiquitin ligase Highwire (Hiw/Phr1). We show that loss of endocytosis causes Hiw to accumulate in neuronal cell bodies, leading to elevated MAP3K Wallenda (Wnd)/DLK levels and hyperactivation of JNK signaling. The accumulated Hiw assembles into dynamic liquid–liquid phase-separated condensates, as revealed by their rapid and reversible dissolution with 1,6-hexanediol. Acute blockade of endocytosis using a temperature-sensitive dynamin mutant *Shibire*^{ts} similarly triggered robust Hiw phase separation. We further demonstrate that Rab11-positive recycling endosomes are essential for proper Hiw localization and turnover, directly linking endosomal trafficking to the control of JNK signaling. Finally, we show that both BMP and JNK signaling are necessary and sufficient to guide synaptic morphogenesis at the *Drosophila* NMJ, thereby integrating endocytic trafficking with synaptic growth signaling. Our findings establish endocytosis as a critical regulator of Hiw/Phr1-dependent JNK signaling via liquid–liquid phase separation, with implications that extend beyond synaptic morphogenesis to axon injury and degeneration pathways.

Introduction

Synapse formation, elimination, and remodeling are fundamental processes in neuronal circuit development and are essential for dynamic plasticity that enables adaptation to sensory experience and physiological stress (BASTRIKOVA *et al.* 2008; COLON-RAMOS 2009; YOSHII AND CONSTANTINE-PATON 2010; CHOU *et al.* 2020; BHARMAURIA *et al.* 2022; HEDRICK *et al.* 2024). Disruptions in these pathways are implicated in various neurodevelopmental and neurodegenerative disorders (WASHBOURNE 2015; DEJANOVIC *et al.* 2024). Consequently, these structural changes are tightly controlled by intracellular signaling networks and membrane trafficking pathways that coordinate synaptic growth and maintenance (CRAVEN AND BREDT 1998; DESHPANDE AND RODAL 2016; CHOU *et al.* 2020; JIANG *et al.* 2021). While several core regulators of synaptic growth have been identified, the molecular mechanisms that fine-tune neuronal signaling and integrate them with intracellular trafficking remain incompletely understood.

Endocytosis, particularly CME, plays a central role in synaptic development by regulating receptor trafficking, signal attenuation, and synaptic vesicle recycling (DI FIORE AND DE CAMILLI 2001; ROYLE AND LAGNADO 2003; HEERSSEN *et al.* 2008). For instance, mutations in endocytic components, including Dynamin, Nervous Wreck (Nwk), AP2 subunits, Synj1, or Endophilin, lead to aberrant synaptic growth, characterized by excessive bouton number, altered bouton size, and/or disrupted active zone spacing (DICKMAN *et al.* 2006; O'CONNOR-GILES *et al.* 2008; ZHAO *et al.* 2013; LAUGKS *et al.* 2017). These phenotypes are primarily attributed to hyperactivation of the BMP signaling pathway (KESHISHIAN AND KIM 2004; MCCABE *et al.* 2004). The BMP pathway, activated by muscle-derived Glass bottom boat (Gbb) binding to Thickveins/Saxophone/Wishful thinking (Tkv/Sax/Wit) receptors, induces Smad-mediated gene expression that promotes synaptic growth (MCCABE *et al.* 2003; GOOLD AND DAVIS 2007; BALL *et al.* 2010; RODAL *et al.* 2011; SMITH *et al.* 2012; VANLANDINGHAM

et al. 2013). While endocytosis modulates this signaling by regulating receptor trafficking, and its disruption enhances BMP activity (DICKMAN *et al.* 2006; CHOUDHURY *et al.* 2022), the BMP-independent roles of endocytosis in synapse growth signaling remain largely unknown.

Genetic studies in *Drosophila* indicate that suppressing BMP signaling alone does not fully rescue the synaptic overgrowth observed in endocytic mutants (COLLINS AND DIANTONIO 2007a; CHOUDHURY *et al.* 2022), suggesting that additional, parallel pathways are required to restore normal synaptic morphology. One such pathway is the Wnd/DLK-JNK cascade, which may act as an additional signaling pathway for synaptic remodeling. Consistent with such a hypothesis, Hiw/Phr1 links autophagy and MAP3K signaling by targeting Wnd for degradation (COLLINS *et al.* 2006; WU *et al.* 2007). While autophagy induces synaptic growth by reducing Hiw level (SHEN AND GANETZKY 2009), Hiw negatively regulates synaptic growth by targeting Wnd, a key activator of the JNK pathway, for degradation (COLLINS *et al.* 2006; WU *et al.* 2007). Loss of Hiw leads to persistent JNK activation, NMJ overgrowth, and is similar to endocytic mutant defects. Hiw also promotes the degradation of co-Smad Medea, implicating it as a key regulator of both BMP and JNK pathways (MCCABE *et al.* 2004). While mutations in Medea only partially suppress the synaptic overgrowth, *wnd* mutants completely suppress the synaptic overgrowth observed in the *hiw* mutants (COLLINS *et al.* 2006; COLLINS AND DIANTONIO 2007a). These genetic epistatic studies imply that, similar to *hiw* mutants, endocytic mutants might regulate multiple signaling pathways that restrict synaptic growth.

Here, we identify a previously unrecognized role for endocytic proteins in restricting synaptic growth by regulating the trafficking, localization, and activity of Hiw. Our study reveals that impaired endocytosis leads to the accumulation and mislocalization of Hiw into dense, inactive condensates within neuronal cell bodies. These aberrant Hiw assemblies cannot target Wnd for degradation, resulting in elevated Wnd levels and sustained activation of JNK signaling. We further demonstrate that Rab11-positive recycling endosomes are crucial for Hiw

trafficking, as Rab11 loss recapitulates endocytic mutant phenotypes, including Hiw condensate formation and Wnd upregulation. Our findings support a model in which endocytosis, through Rab11-mediated recycling and autophagy, enables proper localization and turnover of Hiw/Phr1, preventing its sequestration in inactive condensates and thereby limiting Wnd-JNK signaling. Thus, our work expands the functional repertoire of endocytic proteins and underscores their essential role in maintaining synaptic homeostasis.

Results

Endocytic Impairment Drives Hiw/Phr1 Accumulation and Synaptic Overgrowth Independent of Autophagy

Endocytosis is an established regulator of *Drosophila* NMJ growth, in part because defective endocytic machinery elevates retrograde BMP signaling and leads to synaptic overgrowth (O'CONNOR-GILES *et al.* 2008; BALL *et al.* 2010; RODAL *et al.* 2011; CHOUDHURY *et al.* 2022). However, blocking BMP signaling only partially suppresses the overgrowth observed in several endocytic mutants (COLLINS AND DIANTONIO 2007b; CHOUDHURY *et al.* 2022), indicating that additional pathways contribute to this phenotype. This motivated us to investigate whether altered Hiw–dependent JNK signaling contributes to this process. Hiw is one of the key regulators of JNK signaling and synaptic growth (WAN *et al.* 2000; COLLINS *et al.* 2006), and strikingly, endocytic mutants show synaptic phenotypes that closely resemble those observed in *hiw* mutants (WAN *et al.* 2000).

In order to analyze the Hiw/Phr1 levels in the endocytic mutants, we expressed GFP-Hiw in *AP2* and *synj1* mutant neurons. The GFP-Hiw intensity was significantly elevated in the ventral nerve cord (VNC) of the endocytic mutants (Figure 1A-I and 1M). Careful examination of Hiw organization in these mutants revealed formation of large cytoplasmic puncta in motor neuron cell bodies (Figure 1C–K). These Hiw punctae were fewer in number

(Figure 1J) but had a significantly larger size when compared to controls (Figure 1K), suggesting aberrant Hiw accumulation into large assemblies. Importantly, the expression of GFP alone in *AP2* mutants did not induce GFP accumulations or increased GFP intensity, confirming that the phenotype was not due to overexpression artifacts (Figure 1B-K). Consistently, knockdown of other AP2 subunits (AP2α/AP2β) also induced the formation of Hiw puncta in neuronal cell bodies (Figure S1A-D). Concurrently, Hiw levels at NMJ were significantly reduced in *AP2* or *synj1* mutants (Figure S1E-I), suggesting defective trafficking to synaptic terminals.

Autophagy serves as an additional layer of regulation for Hiw and thereby modulates synaptic growth. Under normal conditions, Hiw protein levels are regulated through autophagic degradation (SHEN AND GANETZKY 2009). Our observation of increased Hiw levels and their accumulation in the endocytic mutants, together with the well-established functional interplay between endocytosis and autophagy (TOOZE *et al.* 2014; KAKUTA *et al.* 2017; BIRGISDOTTIR AND JOHANSEN 2020), and the role of CME in autophagosome biogenesis (TIAN *et al.* 2013; SOUKUP *et al.* 2016; KONONENKO *et al.* 2017; HERNANDEZ-DIAZ *et al.* 2022), prompted us to investigate whether autophagy has any role in mediating the synaptic overgrowth in the endocytic mutants. To test this, first we examined autophagy status in *Drosophila* AP2 mutants by assessing Atg8a levels at the NMJ using an Atg8a-GFP reporter (LOW *et al.* 2013; MAUVEZIN *et al.* 2014). We observed a reduction in Atg8a-GFP levels in *AP2* mutant neurons, suggesting that autophagy might be compromised in these mutants (Figure S2). To further assess autophagic flux, we employed the tandem-tagged GFP-mCherry-Atg8a reporter, a well-established marker for assessing autophagic flux *in vivo* (Figure S3A) (DEVORKIN AND GORSKI 2014). Consistently, we found decreased fluorescence of both GFP and mCherry signals in *AP2* mutants (Figure S3B-H). Similar results were obtained in *synj1* mutants (Figure S3E-H), indicating that although autophagic flux *per se* may not be severely impaired, autophagosome

formation is likely compromised in endocytic mutants, leading to reduced autophagy. Next, to determine whether defective autophagy contributes to the synaptic overgrowth phenotype, we genetically manipulated autophagy in *AP2* and *synj1* mutant backgrounds by either overexpressing Atg1 or reducing its dosage ($atg1^{\Delta 3D}/+$) (SHEN AND GANETZKY 2009). Neither manipulation suppressed the NMJ overgrowth phenotype (Figure S4), indicating that while endocytic defects perturb autophagy, this alone does not account for the observed synaptic overgrowth. These findings suggest that autophagy disruption is not the primary cause of synaptic phenotypes in the endocytic mutants.

Hiw/Phr1 Puncta in Endocytic Mutants are Liquid-Liquid Phase-Separated Condensates

Given that compromised endocytosis led to the accumulation of Hiw/Phr1 in large cytoplasmic puncta, we hypothesized that Hiw may possess intrinsic biophysical features that enable phase separation, and that these assemblies might correspond to biomolecular condensates rather than aggregates. To test this, we performed a comparative *in silico* analysis using PLAAC (LANCASTER *et al.* 2014), IUPred2A, and ANCHOR2 (MESZAROS *et al.* 2018), with Ataxin-2 (Atx2) and GFP serving as positive and negative controls, respectively (BAKTHAVACHALU *et al.* 2018) (Figure 2A-B). As expected, GFP exhibited minimal disorder or binding propensity (IUPred2A/ANCHOR2 scores < 0.4 throughout) and a negative log-likelihood ratio (LLR = –9.614) in PLAAC, suggesting a low propensity for condensation. In contrast, Atx2 showed widespread highly disordered regions, with both IUPred2A and ANCHOR2 scores exceeding the threshold across most of the sequence. PLAAC analysis of Atx2 yielded a strong LLR score of 45.352, in line with its known role in RNP granule formation and stress-induced phase separation (BECKER *et al.* 2017; BAKTHAVACHALU *et al.* 2018).

Remarkably, Hiw displayed intermediate but significant aggregation potential. PLAAC analysis identified several Q/N-rich prion-like regions, with an LLR of 14.279, suggesting bona fide prion-like content. IUPred2A and ANCHOR2 predictions showed distinct stretches of high disorder and disordered binding potential, notably within the N-terminal RCC1-like region (residues ~200–400), a central segment (~900–1050), and an extended region between residues 3000–3700 (Figure 2C-D). Compared to Atx2, Hiw harbors fewer but sharper peaks of disorder and interaction propensity, suggesting a modular architecture capable of regulated condensate formation.

To investigate the nature of Hiw puncta in *AP2* mutants, we examined colocalization with endosomal and stress granule markers. Hiw puncta did not colocalize with markers of early (Rab5), late (Rab7), or recycling (Rab11) endosomes (Figure S5A–F"), nor with Caprin-positive stress granules (Figure S5G–H"), excluding classical vesicular or stress granule identities. Hence, we next tested whether Hiw puntae were phase-separated condensates or stable aggregates. Treatment with 1,6-hexanediol, which disrupts weak hydrophobic interactions in liquid-like assemblies (KROSCHWALD *et al.* 2017), caused a rapid, concentration-dependent dissolution of GFP-Hiw puncta (Figure 2E–L and 2P). In contrast, treatment with 2,5-hexanediol, a similar aliphatic alcohol (NAIR *et al.* 2019), did not dissolve the Hiw/Phr1 punctae, strongly supporting that Hiw/Phr1 punctae were LLPS condensates (Figure 2M-P). Importantly, this effect was reversible, as washing out 1,6-HD and incubating the brains in Schneider's media for 2 hrs restored the condensates, indicating that these phase-separated Hiw/Phr1 structures are maintained by dynamic, reversible molecular interactions (Figure 2Q-S). Together these data support that the observed Hiw/Phr1 punctate structures are maintained by weak, reversible interactions characteristic of biomolecular condensates rather than insoluble aggregates.

To further distinguish whether the Hiw accumulation in the cell body reflected an endosomal trafficking or the autophagy-dependent degradation defect, we examined Hiw distribution in pharmacologically induced (using Bafilomycin A1 or Chloroquine) or genetically (*atg1*$^{\Delta 3D}$) autophagy-deficient animals (SCOTT *et al.* 2004). We found that although overall GFP-Hiw fluorescence increased in autophagy-deficient animals, large cytoplasmic puncta were not observed (Figure S6), indicating that endosomal trafficking disruption and not degradation is likely responsible for Hiw phase separation in endocytic mutants.

Together, these results support that: a) the puncta observed in the endocytic mutants represent dynamic, reversible phase-separated condensates; and b) the Hiw condensate formation is independent of autophagy.

Acute Endocytic Block Triggers Phase-separated Hiw/Phr1 Assemblies

We next asked whether acute inhibition of endocytosis was sufficient to drive Hiw/Phr1 condensation. In order to test this, we examined temperature-sensitive *Shibire* (*shi*^{ts}) mutants, which harbor mutations in dynamin that cause a reversible endocytosis block at restrictive temperature (KOSAKA AND IKEDA 1983). Upon shifting the *shi*^{ts} mutant larvae to restrictive conditions, we observed rapid appearance of Hiw puncta within the neuronal cell body (Figure 3B-H'). These assemblies resembled those seen in *σ2-adaptin* (*AP2*) or *synj1* mutants and were absent under permissive conditions (Figure 3A-G'), suggesting that Hiw/Phr1 assemblies arise due to endocytic blockade rather than developmental effects.

We next asked whether Hiw/Phr1 assemblies formed due to an acute endocytic block exhibit liquid-like behaviour. Interestingly, the Hiw/Phr1 puncta induced by acute endocytic blockade dissolved with a temperature shift from restrictive to permissive (Figure 3C-I' and 3J). Moreover, the punctae induced at restrictive temperature were sensitive to 1,6-HD but not to 2,5-HD, supporting that the observed Hiw/Phr1 punctae are biomolecular condensates

(Figure 3K-Q). Together, these results confirm that endocytic impairments sequester Hiw/Phr1 into LLPS-like condensates.

Wnd/DLK Upregulation Drives the Synaptic Overgrowth in Endocytic Mutants

To determine whether the phase-separated Hiw retains its ability to restrain synaptic growth, we analyzed synaptic defects in GFP-Hiw expressing *AP2* mutant and assessed its ability to suppress the overgrowth phenotype. We found that GFP-Hiw failed to suppress the synaptic overgrowth (Figure S7), indicating that the phase-separated Hiw is non-functional and fails to promote degradation of its targets, Wnd and possibly Medea, thereby activating the downstream MAPK and BMP pathways.

Consistent with this, *AP2* mutants showed elevated Wnd levels, which were restored to control upon neuronal expression of a wild-type AP2 transgene (Figure 4A-G). Similarly, *synj1* mutants displayed both Hiw accumulation and increased Wnd level in neuros (Figure 4F-G). Reducing Wnd dosage in either *AP2* or *synj1* mutants significantly suppressed synaptic overgrowth, restoring both bouton number and size toward control values (Figure 4H-P), indicating that Wnd upregulation is a major downstream effector of the synaptic defects in endocytic mutants. These data indicate that an impaired endocytic pathway compromises Hiw function, leading to elevated Wnd and driving synaptic overgrowth.

Endocytosis Restricts JNK Signaling in *Drosophila* Neurons

We next asked whether impaired Hiw function in endocytic mutants leads to activation of downstream Wnd/DLK signaling, a known regulator of synaptic growth through the JNK pathway in *Drosophila* (WAN *et al.* 2000; COLLINS *et al.* 2006). To monitor JNK signaling, we used the *puckered (puc)-lacZ* transcriptional reporter (Figure 5A) (MARTÍN-BLANCO *et al.* 1998; AGNES *et al.* 1999; ZHU *et al.* 2019). Both *AP2* mutants (Figure 5B–G)

and *synj1* mutants showed significantly elevated puc-lacZ expression in the VNC (Figure 5E–G), indicating upregulation of JNK signaling in these endocytic mutants. This observation was further supported by a TRE-DsRed reporter, a synthetic construct that directly reports AP1/JNK activity (Figure 5A) (CHATTERJEE AND BOHMANN 2012). Consistent with a direct upregulation of JNK signaling, TRE-DsRed expression was robustly elevated in both *AP2* and *synj1* mutants (Figure 5H–M). Together, these results suggest that JNK signaling is upregulated in endocytic mutants and may contribute to synaptic overgrowth.

To directly test whether elevated JNK signaling drives synaptic overgrowth, we suppressed this pathway by expressing a dominant-negative form of JNK (bsk^{DN}) or its downstream transcription factor fos^{DN} (kay^{DN}) in *AP2* mutant neurons. These genetic manipulations significantly suppressed synaptic overgrowth in the endocytic mutants (Figure 6A–F, I–J), supporting a causal role for JNK signaling in restricting synaptic growth.

However, either bsk^{DN} or kay^{DN} is not able to rescue the synaptic overgrowth completely to the control levels. Because endocytosis is also known to attenuate BMP signaling and restrict synaptic growth (WU *et al.* 2005b; O'CONNOR-GILES *et al.* 2008; GLEASON *et al.* 2014; JACOMIN *et al.* 2015; EHRLICH 2016; GLEASON *et al.* 2017), we asked whether JNK and BMP pathways function in the same pathway or independently to restrict synapse growth. To dissect their respective contributions, we co-express a dominant-negative form of Kay alongside a loss-of-function allele of Tkv ($tkv^{7/+}$), a BMP receptor, in *AP2* mutants. Strikingly, this combination fully suppressed both the increased bouton number and size, restoring them to the wild-type levels (Figure 6G-J). Together, these findings suggest that JNK and BMP signaling pathways act in parallel to induce synaptic overgrowth when endocytosis is impaired and that simultaneous attenuation of both pathways is necessary and sufficient to normalize synaptic growth.

Loss of Rab11 Promotes Hiw/Phr1 Phase Separation and Activates JNK Pathway Akin to Endocytic Mutants

While phase-separated Hiw accumulates in endocytic mutants, autophagy-deficient mutants show no such cytoplasmic Hiw assemblies despite elevated total Hiw levels (Figure S6E-I). This observation suggests that reduced Hiw degradation alone is not sufficient for condensate formation and that trafficking defects could be a critical determinant of Hiw phase separation in endocytic mutants. Hence, to directly test whether Hiw trafficking involves the endosomal system, we neuronally expressed dominant-negative (DN) forms of the small GTPases Rab5, Rab7, or Rab11, which regulate different steps of endocytosis and recycling. While expression of DN-Rab5 ($Rab5^{S43N}$) or DN-Rab7 ($Rab7^{T22N}$) did not affect Hiw localization in neurons, expression of DN-Rab11 ($Rab11^{S25N}$) resulted in its phase-separation and accumulation within neuronal cell bodies, phenocopying the endocytic mutants (Figure 7A-E).

Consistent with these findings, *Rab11* mutants also displayed both Hiw condensates and elevated levels of Hiw substrate Wnd/DLK (Figure 7F-O and Figure S8). Strikingly, synaptic overgrowth in *Rab11* mutants was significantly suppressed by neuronal expression of dominant-negative bsk^{DN} or dominant-negative kay^{DN} (Figure 8A-F), suggesting that JNK pathway activation lies downstream to Rab11 activity. These genetic epistatic interactions suggest that the disrupted Rab11-dependent recycling impedes proper localization of Hiw, thereby triggering aberrant JNK signaling and synaptic overgrowth. Given that Rab11-positive recycling endosomes are reduced in both *AP2* and *synj1* mutants (CHOUDHURY *et al.* 2022), these findings suggest that Rab11-dependent endosomal recycling normally maintains the proper localization/trafficking of Hiw, and its dysfunction contributes to Hiw phase separation, functional inactivation, and subsequent JNK pathway hyperactivation in endocytic mutants and synaptic overgrowth.

Discussion

Endocytosis is increasingly recognized as a key modulator of neuronal signalling beyond its canonical roles in vesicle recycling (COSKER AND SEGAL 2014). Here, we identify a previously unrecognized function of endocytic trafficking in constraining synaptic growth by preventing aberrant phase separation of E3 ubiquitin ligase Highwire. When endocytic recycling is compromised, Hiw trafficking is disrupted, leading to its liquid-liquid phase separation and functional inactivation. This loss in Hiw activity causes Wnd/DLK upregulation and JNK hyperactivation, resulting in synaptic overgrowth independent of autophagic dysfunction. Moreover, we identify Rab11-dependent recycling as a critical mediator of Hiw trafficking, which prevents Hiw mislocalization and phase separation.

A Role for Endocytosis in Regulating Synaptic Stability by Modulating Hiw/Phr1 Function

Prior studies proposed that synaptic overgrowth observed in autophagy mutants arises from reduced Hiw turnover (SHEN AND GANETZKY 2009). However, paradoxically, *AP2* and *synj1* mutants exhibit Hiw accumulation as puncta in the neuronal cell bodies, aberrantly elevated JNK signaling, and synaptic overgrowth, phenotypes that are consistent with reduced Hiw/Phr1 function.

Our data reveal that endocytic proteins serve a broader role beyond synaptic vesicle recycling. Endocytosis ensures proper trafficking and spatial availability of regulatory proteins such as Hiw/Phr1. We provide several lines of evidence to support this conclusion: a) acute disruption of CME via temperature-sensitive paralytic mutant *shibire*^{ts} causes Hiw mislocalization and puncta formation; b) loss of recycling endosomal GTPase Rab11 phenocopies these defects, directly implementing endosomal recycling in Hiw regulation; and c) the puncta represent non-vesicular liquid-liquid phase-separated condensates, rather than

degradation intermediates, indicating that Hiw is sequestered rather than degraded under endocytic/trafficking block. Thus, endocytosis positions Hiw near its neuronal substrates by protecting it from aberrant sequestration, a mechanism consistent with broader observations that disruption of membrane trafficking can mislocalize critical signaling molecules in neurons (LEITCH *et al.* 2014). Since neuronal morphology and function depend on spatially restricted signaling, CME likely contributes to synaptic stability by protecting key regulatory complexes, such as Hiw/Phr1, from phase separation-driven spatial miscompartmentalization.

These findings place Hiw/Phr1 within a growing class of neuronal proteins that undergo biomolecular condensation to regulate synaptic structure and function. For example, post-synaptic scaffolds such as PSD-95 and SynGAP form LLPS condensates to assemble post-synaptic densities and tune synaptic plasticity (ZENG *et al.* 2016). Similarly, presynaptic scaffolds such as SYD-2/Liprin-α and ELKS undergo LLPS to establish active zones in *C. elegans* and mammals (MCDONALD *et al.* 2020). Our data extends LLPS-regulated structural scaffold organization to E3-ubiquitin ligase, showing that phase separation can regulate signaling hubs that control neuronal growth and morphogenesis. Our findings highlight an underappreciated layer of regulation where membrane trafficking intersects with LLPS to spatially gate enzymatic activity to regulate neuronal signaling.

Autophagy-Endocytosis Crosstalk Regulates Highwire Compartmentalization and Synaptic Homeostasis

While autophagy facilitates the turnover of synaptic signaling proteins (SHEN AND GANETZKY 2009; HOFFMANN-CONAWAY *et al.* 2020), endocytosis controls autophagic flux by regulating membrane supply and the trafficking of autophagy-related proteins (BIRGISDOTTIR AND JOHANSEN 2020; ANDRES-ALONSO *et al.* 2021). Endosomes are a primary membrane source for autophagosome formation (RAVIKUMAR *et al.* 2010; PURI *et al.* 2013; BIRGISDOTTIR AND JOHANSEN 2020), linking autophagic processes to endocytic flux. Endocytic proteins such

as AP2 and Synj1 also modulate autophagy through endocytosis-independent mechanisms, particularly at the synaptic terminals (VANHAUWAERT *et al.* 2017; BERA *et al.* 2020). Thus, autophagy defects in endocytic mutants may arise from defective membrane supply and direct regulatory functions of endocytic proteins on autophagic machinery. Our analysis reveals that endocytosis and endosomal trafficking, but not autophagy, are essential to prevent aberrant phase separation of Hiw into large puncta within neuronal cell bodies. These condensates, solubilized by 1,6-hexanediol (KROSCHWALD *et al.* 2017) (Figure 2E-S), are not part of the endosomes or stress granules and are absent in autophagy-deficient animals (Figure S5 and Figure S6). In autophagy mutants such as $Atg1^{\Delta 3D}$/+, we observed elevated steady-state Hiw levels, consistent with impaired degradation, but no Hiw puncta formation. Similarly, pharmacological inhibition of autophagy increased total Hiw abundance but did not promote condensates. Thus, autophagy determines Hiw abundance, while endocytic trafficking determines its spatial distribution and LLPS behaviour.

Our data that acute disruption of CME in shi^{ts} mutants was sufficient to trigger rapid Hiw phase separation into large cytoplasmic punctae (Figure 3A-J) further supports the view that endocytosis maintains Hiw in a soluble, spatially accessible pool. Autophagy alone is insufficient to control Hiw/Phr1 distribution. This separation of roles supports a two-tiered control of Hiw/Phr1 regulation: while autophagy limits Hiw/Phr1 levels, endocytosis prevents its aberrant phase separation. While we cannot exclude indirect contributions of autophagy impairments under these conditions, the absence of puncta in autophagy-deficient animals strongly argues that autophagic inhibition alone is insufficient to induce Hiw phase separation. These results reveal that endocytosis maintains synaptic homeostasis by regulating Hiw in a spatially accessible, non-condensed pool. While autophagy controls total Hiw protein levels, only endocytic trafficking prevents its aberrant sequestration into phase-separated assemblies, thereby restricting Hiw-mediated synaptic growth.

Rab11-Dependent Endosomal Recycling: Essential Spatial Control Node for Hiw/Phr1 Trafficking and JNK Signaling

Rab11-positive recycling endosomes serve as dynamic platforms that integrate endocytosis, membrane recycling, and autophagy. They not only contribute to autophagosome biogenesis by supplying membrane and trafficking autophagy-related proteins but also play essential roles in receptor trafficking and synaptic homeostasis (ULLRICH *et al.* 1996; GREEN *et al.* 1997; WILCKE *et al.* 2000; BARTZ *et al.* 2003; LONGATTI *et al.* 2012; LONGATTI AND TOOZE 2012; ZULKEFLI *et al.* 2019). In *Drosophila*, Rab11 cooperates with Nwk to regulate BMP receptor recycling, actin dynamics, and synaptic growth signaling at the NMJ (RODAL *et al.* 2008). Similarly, *AP2* and *Synj1* mutants genetically interact with *Rab11* mutants, and Rab11 levels are significantly reduced at the *AP2* mutant synapses, implicating endocytic recycling as a key signalling integration node between CME and autophagic flux (CHOUDHURY *et al.* 2022).

In *C. elegans*, the E3 ubiquitin ligase RPM-1 regulates synaptic development through interactions with the Rab GTPase GLO-1 and its GEF GLO-4 via late endosomes, suggesting that endosomal pathways help spatially restrict RPM-1 function within neurons (GRILL *et al.* 2007; OPPERMAN AND GRILL 2014b). While the specific endosomal compartment may differ across species, our findings in *Drosophila* similarly implicate endosomal trafficking in the localization and function of Hiw, the RPM-1 ortholog. Our data reveal that Rab11-mediated endosomal recycling is an essential trafficking event preventing Hiw condensation.

A recent finding suggest that Rab11 is a critical mediator in the anterograde transport and sorting of Wnd to axon terminals for degradation, and that disruptions of this process lead to Wnd accumulation, excessive stress signaling, and neuronal degeneration (KIM *et al.* 2024). Our study offers an alternate/additional mechanism for these observations and supports the idea that loss of Rab11 renders Hiw inactive by promoting phase separation, thereby leading to

elevated Wnd levels. Together with CME, Rab11-positive endosomes form a trafficking axis that regulates the spatial dynamics and functional availability of Hiw, preventing overactivation of JNK activity and restricting synapse overgrowth. The JNK signaling has long been implicated in regulating synaptic expansion, plasticity, and dendritic architecture across species, from *Drosophila* to mammals (WU *et al.* 2005a; ABRAMS *et al.* 2008; OPPERMAN AND GRILL 2014a). The genetic suppressions of JNK signaling by blocking the components of the JNK pathway or Wnd mutants demonstrate that synaptic overgrowth in endocytic mutants is directly mediated by JNK pathway activation downstream of Wnd (Figures 4 and 6). Notably, combined inhibition of JNK and BMP pathways in endocytic mutants or Rab11 mutants fully restores synaptic morphology, indicating that JNK acts in parallel, not simply downstream, to BMP in restricting synaptic growth, supporting emerging models that growth-promoting pathways integrate in a context-dependent, multi-pathway framework.

We suggest a dual safeguarding model (Figure 8G) in which endocytosis and Rab11-mediated recycling endosomes spatially govern Hiw distribution, preventing its sequestration into phase-separated condensates. Autophagy provides complementary support for Hiw turnover. Together, these mechanisms maintain a critical threshold for Wnd-JNK signaling in neurons and restrict synaptic overgrowth.

Our study adds to a growing consensus that LLPS is not limited to synaptic scaffolds or RNA granules but also controls neuronal signaling hubs. The conservation of Hiw/Phr1-JNK pathway suggests a fundamental cellular logic linking membrane trafficking, biomolecular condensation, and E3-ubiquitin-dependent signaling in the regulation of neuronal growth and plasticity. Beyond developmentally regulated synapse growth, our findings may have implications for axon regeneration, where defects in endocytosis/endosomal trafficking accelerate JNK-driven neuronal loss and synaptic collapse.

Materials and Methods

Fly Stocks

All the flies were grown and maintained at 25°C temperature in a standard cornmeal medium as described previously (CHOUDHURY *et al.* 2016). w^{1118} was used as a control unless otherwise mentioned. Both males and females were used for experiments. The *AP2σ* mutant alleles used were $AP2\sigma^{ang7}$, a hypomorphic allele generated through P-element mobilization of $Synd^{EP877}$ located 2416 bp upstream of Syndapin ORF, and $AP2\sigma^{KG0245}$, a null allele of AP2σ which has a P-element insertion in the third exon of AP2σ ORF (CHOUDHURY *et al.* 2016). The following fly stocks were obtained from BDSC: $AP2\sigma^{KG02457}$ (BL13478), *UAS-GFP-mCherry-Atg8a* (BL37749), *UAS-GFP-Atg8a* (BL52005), *UAS-GFP-Hiw* (BL51639), *UAS-AP2β RNAi* (BL28328), *UAS-Atg1* (BL51654) $UAS\text{-}bsk^{DN}$ (BL6409), $UAS\text{-}kay^{DN}$ (BL7214), $synj1^{1}$ (BL24883), $synj1^{2}$ (BL24884), tkv^{7} (BL3242), wnd^{2}, wnd^{3} (BL51999) (COLLINS *et al.* 2006), TRE-DsRed (BL59011), $UAS\text{-}Rab5^{S43N}$ (BL42703), $UAS\text{-}Rab7^{T22N\text{-}YFP}$ (BL9778), and $UAS\text{-}Rab11^{S25N\text{-}YFP}$ (BL23261). Other lines used in the study are: $atg1^{\Delta 3D}$ *(SCOTT et al. 2004)*, *UAS-AP2α RNAi* (GD15566), $Rab11^{93Bi}$, and $Rab11^{ex2}$ (KHODOSH *et al.* 2006), *puc-lacZ* (RING AND MARTINEZ ARIAS 1993).

The shi^{ts1} and shi^{ts2} temperature-sensitive mutant fly stocks were maintained at 18°C, and experimental crosses were set up at the permissive temperature of 20°C. Once the progeny reached the wandering third instar larval stage, larvae were shifted to the non-permissive temperature of 29°C for 6 hours to induce acute disruption of dynamin-mediated endocytosis (KOSAKA AND IKEDA 1983; DICKMAN *et al.* 2006; KROLL *et al.* 2015).

Immunohistochemistry and Imaging

Third instar wandering larvae were dissected in cold, calcium-free HL3 saline (pH 7.2) containing 70 mM NaCl, 5 mM KCl, 20 mM $MgCl_2$, 10 mM $NaHCO_3$, 5 mM Trehalose, 115 mM sucrose, and 5 mM HEPES and fixed in 4% paraformaldehyde for 30 min. Fillets were

washed in PBS containing 0.2 % Triton X-100, blocked for one hour with 5% bovine serum albumin (BSA), and then incubated overnight with the primary antibody at 4°C. The primary antibodies used in the study are mouse anti-CSP (1:50) (DSHB, Iowa city, USA), mouse anti-NC82 (1:100) (DSHB), rat anti-Elav (1:200) (DSHB), mouse anti-β-galactosidase (1:200) (DSHB), rabbit anti-Wallenda (1:100, (COLLINS *et al.* 2006)), guinea pig anti-Rab5 (1:500) (MOTTOLA *et al.* 2010) was a gift from Marino Zerial (Max Planck Institute, Germany), rabbit anti-Rab7 (1:500) and rabbit anti-Rab11 (1:500); (TANAKA AND NAKAMURA 2008; WEST *et al.* 2015) antibodies were a gift from Tsubasa Tanaka (RIKEN Center for Developmental Biology, Japan). Rabbit anti-Caprin (1:200) was a gift from Ophelia Papoulas (University of Texas, (PAPOULAS *et al.* 2010). The secondary antibodies conjugated to Alexa Fluor 488, Alexa Fluor 568, and Alexa Fluor 633 (Invitrogen, ThermoFisher Scientific, Waltham, MA, USA) were used at a 1:800 dilution. The Alexa Fluor 488 or Rhodamine-conjugated anti-HRP (Jackson ImmunoResearch, Pennsylvania, USA) was used at a 1:800 dilution.

For Wnd staining, larvae were dissected in ice-chilled 1X PBS and fixed in 3.7% formalin on ice for one hour. Larval fillets were blocked with 5% BSA for 1 hour, followed by overnight incubation with primary antibody anti-Wnd and anti-NC82 at 4°C (COLLINS *et al.* 2006). For GFP-mCherry-Atg8a staining, the larvae were dissected in cold, calcium-free HL3 saline and fixed for 15 minutes at room temperature in 4% PFA in PBS (pH 7.2). Larval fillets were mounted in VECTASHIELD (Vector Laboratories, California, USA), and images were captured with a laser scanning confocal microscope (FV3000, Olympus Corporation, Tokyo, Japan).

Hexanediol treatment

Third instar *Drosophila* larvae expressing GFP-Hiw were dissected in cold Schneider's *Drosophila* Medium (Gibco). Following dissection, preparations were gently washed with fresh Schneider's medium to remove residual debris. To assess the solubility

properties of accumulated Hiw, preparations were incubated for 2 minutes at room temperature in Schneider's medium containing 1,6-hexanediol (1,6-HD; Sigma-Aldrich, #H6703) or 2,5-HD (Sigma-Aldrich, #H11904) at final concentrations of 0%, 1%, 5%, or 10%. The 0 % condition consisted of Schneider's medium alone (LIU *et al.* 2020). Following treatment, samples were immediately fixed in 4% paraformaldehyde in PBS for 30 minutes at room temperature. Fixed tissues were then washed and processed for immunostaining. No antibody amplification was used for GFP. The drug-containing medium was replaced with normal Schneider's medium for 2h for recovery before fixation.

Western Blotting

Third instar larval *Drosophila* brains were homogenized in 1× SDS lysis buffer (50 mM Tris-Cl, pH 6.8; 25 mM KCl; 2 mM EDTA; 0.3 M sucrose; 2% SDS). The protein concentration was determined using the bicinchoninic acid (BCA) protein assay. Homogenates were mixed with an equal volume of 2× Laemmli buffer (50 mM Tris-HCl, pH 6.8; 2% SDS; 2% β-mercaptoethanol; 0.1% bromophenol blue; 10% glycerol), and 30 μg of protein was loaded onto a 5% SDS-PAGE gel. Proteins were transferred to a Hybond-LFP PVDF membrane (GE Healthcare, Illinois, USA). Membranes were blocked in 5% skimmed milk in 1× Tris-buffered saline containing 0.2% Tween-20 (0.2% TBST) for 1 hour at room temperature and incubated overnight at 4°C with primary antibody mouse anti-GFP (1:2000) and anti-Ran (1:2000, BD Biosciences, New Jersey, USA). After washing with 0.2% TBST, membranes were incubated with HRP-conjugated secondary antibody for 1 hour at room temperature. Signals were detected using the LI-COR Odyssey imaging system (LI- COR Biosciences, Lincoln, USA).

Bafilomycin A1 and Chloroquine Treatment

To pharmacologically inhibit lysosomal function, third instar *Drosophila* larvae expressing GFP-Hiw were transferred to standard fly food containing either 200 nM

Bafilomycin A1 (Baf) for 6 hours or 2.5 mg/ml Chloroquine (CQ) for 24 hours at 25°C. Stock solutions of both compounds were prepared in DMSO, and larvae fed on DMSO alone were served as controls. After the treatment, larvae were dissected in cold, calcium-free HL3 saline (pH 7.2) and proceeded with the immunocytochemistry protocol (ZIRIN *et al.* 2013; MAUVEZIN *et al.* 2015).

Quantifications and Statistical Analysis

NMJ 6/7 from the A2 hemisegment were captured to calculate the bouton number. All the CSP-positive boutons were counted manually in ImageJ/Fiji software (National Institutes of Health, Bethesda, USA). The number of boutons from each NMJ was normalized to the respective muscle area. For muscle area quantification, images from the A2 hemisegment were captured using a 20× objective, and the area was quantified using ImageJ/Fiji software. For bouton area quantification, all terminal type-II boutons from muscle 6/7 at A2 hemisegment were used, and the bouton area was calculated by drawing a free-hand sketch around CSP-positive boutons using ImageJ. NMJs from muscle 4 were captured using a plan apochromat 60×, 1.42 NA objective for fluorescence intensity quantification. All the control and experimental fillets were processed similarly for each NMJ, and the fluorescence images were captured under the same settings for a particular experimental set. The average intensity was normalized to the control intensity. The average fluorescence intensity of GFP was normalized with that of mCherry for the analysis of autophagy flux.

To quantify the GFP-Hiw puncta number and size, z-projections of confocal images of third-instar larval VNCs were captured and stacked. The Gaussian filter was applied to the images and thresholded. The analyzed particle function of ImageJ was used to quantify the number of puncta and their size. For Hiw intensity quantification, the individual VNC of all genotypes was captured with the same parameters, the region of interest (whole VNC) was manually selected, and the integrated density was calculated using ImageJ and divided by the

area of the ROI to obtain the average integrated density or the average fluorescence intensity. Similarly, individual neuronal cell bodies were marked using the GFP (*UAS-GFP*) positive area and added to the ROI manager. Using the ROI area, the intensity of GFP-Hiw and Elav was quantified for each neuronal cell body, averaged, and normalized. The NC82 positive area was marked as ROI, and the mean intensity was measured for Wnd and normalized with the corresponding NC82 intensity. To quantify the *puc-LacZ* and *TRE-DsRed* expression, Elav-positive nuclei were marked in the z-stack images of the third instar larval VNCs, and the levels of *puc-LacZ* and *TRE-DsRed* were quantified and normalized with the corresponding Elav levels (XIONG *et al.* 2010). When quantifying the individual neuronal intensity, the corresponding Elav intensity was used for the normalization, and for whole VNC quantification, the overall Elav intensity was used.

The density of Western blot bands was quantified using ImageJ software. For multiple comparisons, one-way ANOVA followed by post hoc Tukey's or Student's t-test was used. GraphPad Prism 8 (GraphPad Software Inc., California, USA) was used to plot all the graphs. Error bars in all the histograms represent SEM. $*p < 0.05$, $**p < 0.01$, $***p < 0.001$, ns; not significant.

Aknowledgments

We thank Dr. Avital Rodal for sharing *rab11* mutants, Dr. Mohit Prasad for sharing the *puc-lacZ* fly lines, and Dr. Guang-Chao Chen for the *atg1* mutant lines. We also thank Dr. Aaron DiAntonio and Dr. Catherine Collins for generously sharing the Wallenda antibody, Dr. Tsubasa Tanaka for Rab7 and Rab11 antibodies, Dr. Marino Zerial for Rab5 antibodies, Dr. Ophelia Papoulas for sharing the Caprin antibody; the BDSC for the fly stocks; DSHB, the University of Iowa for monoclonal antibodies; and Varun Chaudhary, Sunando Datta and Catherine Collins for their helpful comments on this manuscript. We thank the DST-FIST program of the Government of India for providing a confocal microscope to IISER-Bhopal. This work was supported by the Science and Engineering Board (SERB) Project Grant CRG/2021/000599, the Government of India, and by intramural funds from the Indian Institute of Science Education and Research Bhopal to V.K.

Data availability

All data related to this manuscript are contained within the article.

Figure Legends

Figure 1: Compromised endocytosis causes Hiw to accumulate in large assemblies within the neuronal cell body

(**A**) Schematic representation of the third instar larval ventral nerve cord (VNC). The magnified view represents accumulation and possible mislocalization of the Hiw assemblies in the neuronal cell bodies of endocytic mutants.

(**B-G''**) Confocal images of the neuronal cell body in third instar larval VNC co-labeled for GFP-Hiw (green) and Elav (magenta) in GFP control (*Elav-Gal4>UAS-GFP)* (B-B''), *Elav-Gal4>UAS-GFP-Hiw* (C-C''), *Elav-Gal4>UAS-GFP; AP2σ-^{KG02457}/AP2σ^{ang7}* (D-D''), *Elav-Gal4>UAS-GFP-Hiw; AP2σ-^{KG02457}/AP2σ^{ang7}* (E-E''), *Elav-Gal4>UAS-GFP-Hiw; UAS-AP2σ, AP2σ-^{KG02457}/AP2σ^{ang7}* (F-F''), and *Elav-Gal4>UAS-GFP-Hiw; synj1$^{1/2}$* (G-G''). The scale bar in G'' represents 5 µm.

(**H**) Histogram showing the average intensity of GFP-Hiw in third instar larval VNC in GFP control (*Elav-Gal4>UAS-GFP*) (1.07 ± 0.03), *Elav-Gal4>UAS-GFP-Hiw* (0.95 ± 0.08), *Elav-Gal4>UAS-GFP; AP2σ-^{KG02457}/AP2σ^{ang7}* (1.10 ± 0.04), *Elav-Gal4>UAS-GFP-Hiw; AP2σ-^{KG02457}/AP2σ^{ang7}* (2.52 ± 0.10), *Elav-Gal4>UAS-GFP-Hiw; UAS-AP2σ, AP2σ-^{KG02457}/AP2σ^{ang7}* (0.97 ± 0.07), and *Elav-Gal4>UAS-GFP-Hiw; synj1$^{1/2}$* (1.94 ± 0.13). At least 10 VNCs of each genotype were used for the quantifications.

(**I**) Histogram showing the average intensity of GFP-Hiw in individual neuronal cell body in GFP control (*Elav-Gal4>UAS-GFP*) (1.65 ± 0.08), *Elav-Gal4>UAS-GFP-Hiw* (0.45 ± 0.02), *Elav-Gal4>UAS-GFP; AP2σ-^{KG02457}/AP2σ^{ang7}* (1.53 ± 0.11), *Elav-Gal4>UAS-GFP-Hiw; AP2σ-^{KG02457}/AP2σ^{ang7}* (1.13 ± 0.04), *Elav-Gal4>UAS-GFP-Hiw; UAS-AP2σ, AP2σ-^{KG02457}/AP2σ^{ang7}* (0.62 ± 0.02), and *Elav-Gal4>UAS-GFP-Hiw; synj1$^{1/2}$* (1.15 ± 0.09). At least 10 VNCs of each genotype were used for the quantifications.

(**J**) Histogram showing the number of GFP-Hiw puncta in GFP control (*Elav-Gal4>UAS-GFP*) (7.00 ± 1.48), *Elav-Gal4>UAS-GFP-Hiw* (806.6 ± 35.31), *Elav-Gal4>UAS-GFP; AP2σ-^{KG02457}/AP2σ^{ang7}* (8.500 ± 1.37), *Elav-Gal4>UAS-GFP-Hiw; AP2σ-^{KG02457}/AP2σ^{ang7}* (159.3 ± 16.52), *Elav-Gal4>UAS-GFP-Hiw; UAS-AP2σ, AP2σ-^{KG02457}/AP2σ^{ang7}* (851.9 ± 28.73), and *Elav-Gal4>UAS-GFP-Hiw; synj1$^{1/2}$* (150.9 ± 7.66). At least 10 VNCs of each genotype were used for the quantifications.

(**K**) Histogram showing the size of GFP-Hiw puncta in GFP control (*Elav-Gal4>UAS-GFP*) (0.01 ± 0.002), *Elav-Gal4>UAS-GFP-Hiw* (0.06 ± 0.01), *Elav-Gal4>UAS-GFP; AP2σ-^{KG02457}/AP2σ^{ang7}* (0.01 ± 0.001), *Elav-Gal4>UAS-GFP-Hiw; AP2σ-^{KG02457}/AP2σ^{ang7}* (0.20 ± 0.01), *Elav-Gal4>UAS-GFP-Hiw; UAS-AP2σ, AP2σ-^{KG02457}/AP2σ^{ang7}* (0.11 ± 0.01), and *Elav-Gal4>UAS-GFP-Hiw; synj1$^{1/2}$* (0.21 ± 0.004). At least 10 VNCs of each genotype were used for the quantifications.

The error bar in H, I, J, and K represents the standard error of the mean (SEM); the statistical analysis was done using one-way ANOVA followed by post hoc Tukey's test. ***p<0.001, ns: not significant.

(**L**) Western blot showing the level of GFP-Hiw in control (*Elav-Gal4>UAS-GFP-Hiw*), *Elav-Gal4>UAS-GFP-Hiw; AP2σ-^{KG02457}/AP2σ^{ang7}*, *Elav-Gal4>UAS-GFP-Hiw; UAS-AP2σ, AP2σ-^{KG02457}/AP2σ^{ang7}*, and *Elav-Gal4>UAS-GFP-Hiw; synj1$^{1/2}$*. Ran was used as a loading control.

(**M**) Histogram showing the level of GFP-Hiw in control (*Elav-Gal4>UAS-GFP-Hiw*) (1.0 ± 0.00), *Elav-Gal4>UAS-GFP-Hiw; AP2σ-^{KG02457}/AP2σ^{ang7}* (1.73 ± 0.06), *Elav-Gal4>UAS-GFP-Hiw; UAS-AP2σ, AP2σ-^{KG02457}/AP2σ^{ang7}* (1.02 ± 0.12), and *Elav-Gal4>UAS-GFP-Hiw; synj1$^{1/2}$* (1.53 ± 0.02). Three independent Western blots were used for quantification. The error bar represents the standard error of the mean (SEM); the statistical analysis was done using one-way ANOVA followed by post hoc Tukey's test. ***p<0.001; **p<0.01.

Figure 2: Highwire assembles as dynamic condensates in endocytic mutants

(**A-C**) The PLAAC scores of GFP, Atx2, and Hiw. The PLAAC scores represent the ability of a protein segment to form aggregates or LLPS (LANCASTER *et al.* 2014). The plots represent predicted intrinsically disordered regions in a protein. The red line denotes the likelihood of a protein segment being disordered. The blue line denotes the probability of a given position in a protein being a part of a disordered binding region.

(**D**) The domain organization of Hiw protein. It contains an N-terminal RCC1-like domain (RLD), two (PAM-Hiw-RPM-1) PHR domains, followed by (Rae1-binding domain) RBD and (Fsn-1 binding domain) FBD1, and a C-terminal (RING H2 ubiquitin-ligase domain) RING domain.

(**E-L''**) Confocal images of the neuronal cell body co-labelled for GFP-Hiw (green) and Elav (magenta) in control (*Elav-Gal4>UAS-GFP-Hiw*) and *Elav-Gal4>UAS-GFP-Hiw; AP2σ-^{KG02457}/AP2σ^{ang7}* treated with 0% 1,6-HD (E-F''), 1% 1,6-HD (G-H''), 5% 1,6-HD (I-J''), and 10% 1,6-HD (K-L'') containing Schneider's media for 2 mins. The 0% contains only media. The scale bar in L'' represents 5 µm for images E-L''.

(**M-O''**) Confocal images of the neuronal cell body co-labelled for GFP-Hiw (green) and Elav (magenta) in *Elav-Gal4>UAS-GFP-Hiw; AP2σ-^{KG02457}/AP2σ^{ang7}* treated with 1% 2,5-HD (M-M''), 5% 2,5-HD (N-N''), and 10% 2,5-HD (O-O'') containing Schneider's media for 2 mins. The scale bar in O'' represents 5 µm for images M-O''.

(**P**) Line graph showing the average size of the GFP-Hiw punctae in control (*Elav-Gal4>UAS-GFP-Hiw*) (black line) and *Elav-Gal4>UAS-GFP-Hiw; AP2σ^{KG02457}/AP2σ^{ang7}* treated with 0%, 1%, 5% and 10% 1,6-HD (blue line), and *Elav-Gal4>UAS-GFP-Hiw; AP2σ^{KG02457}/AP2σ^{ang7}* treated with 1%, 5% and 10% 2,5-HD (orange line).

(**Q-R''**) Confocal images of the neuronal cell body co-labelled for GFP-Hiw (green) and Elav (magenta) in *Elav-Gal4>UAS-GFP-Hiw; AP2σ-^{KG02457}/AP2σ^{ang7}* treated with 5% 1,6-HD for 2

min and allowed to recover for 2 hrs after removal of 1,6-HD in S2 Schneider's media. The scale bar in R'' represents 5 µm.

(**S**) Histogram showing the size (in µm) of GFP-Hiw puncta in *Elav-Gal4>UAS-GFP-Hiw; AP2σ-^{KG02457}/AP2σ^{ang7}* treated with 5% 1,6-HD for 2 min (0.076 ± 0.005), and *Elav-Gal4>UAS-GFP-Hiw; AP2σ-^{KG02457}/AP2σ^{ang7}* after recovery for 2 hrs (0.133 ± 0.003). At least 8 VNCs of each genotype were used for the quantifications. The error bar represents the standard error of the mean (SEM); the statistical analysis was done using Student's t-test. ***p<0.001.

Figure 3: Acute inhibition of endocytosis triggers Hiw/Phr1 condensate formation

(**A-I'**) Confocal images of the neuronal cell body co-labelled for GFP-Hiw (green) and Elav (magenta) in control (*Elav-Gal4>UAS-GFP-Hiw*) (A-C'), *Elav-Gal4>UAS-GFP-Hiw; shi^{ts1}* (D-F'), and *Elav-Gal4>UAS-GFP-Hiw; shi^{ts2}* (G-I'). The scale bar in I' represents 5 µm.

(**J**) Histogram showing the average size of GFP-Hiw puncta in control, *Elav-Gal4>UAS-GFP-Hiw; shi^{ts1}*, and *Elav-Gal4>UAS-GFP-Hiw; shi^{ts2}* at permissive (20 °C) and restrictive temperatures (29 °C). At least 8 VNCs of each genotype were used for the quantifications.

(**K-P'**) Confocal images of the neuronal cell body co-labelled for GFP-Hiw (green) and Elav (magenta) in *Elav-Gal4>UAS-GFP-Hiw, and Elav-Gal4>UAS-GFP-Hiw; AP2σ-^{KG02457}/AP2σ^{ang7}* treated with 5% 2,5-HD and 1,6-HD for 2 min. The scale bar in P' represents 5 µm.

(**Q**) Histogram showing the average size of GFP-Hiw puncta in untreated, 5% 2,5-HD, and 5% 1,6-HD treated control, *Elav-Gal4>UAS-GFP-Hiw; shi^{ts1}*. At least 8 VNCs of each genotype were used for the quantifications.

Figure 4: Endocytosis restricts synaptic growth via MAP3K/Wnd signaling

(**A-F''**) Confocal images of third instar larval ventral nerve cord co-labelled for Wnd (magenta) and NC82 (green) in control (A-A''), *Elav-Gal4>UAS-GFP-Hiw* (B-B''), *AP2σ-^{KG02457}/AP2σ^{ang7}* (C-C''), *Elav-Gal4>UAS-AP2σ, AP2σ-^{KG02457}/AP2σ^{ang7}*(D-D''), *Elav-Gal4>UAS-GFP-Hiw; AP2σ-^{KG02457}/AP2σ^{ang7}* (E-E''), and (F-F'') *Elav-Gal4>UAS-GFP-Hiw; synj1$^{1/2}$*. The scale bar in F'' represents 20 µm.

(**G**) Histogram showing the average fluorescence intensity of Wnd in control (0.76 ± 0.04), *Elav-Gal4>UAS-GFP-Hiw* (0.51 ± 0.01), *AP2σ-^{KG02457}/AP2σ^{ang7}* (1.46 ± 0.05), *Elav-Gal4>UAS-AP2σ, AP2σ-^{KG02457}/AP2σ^{ang7}* (0.70 ± 0.05), *Elav-Gal4>UAS-GFP-Hiw; AP2σ-^{KG02457}/AP2σ^{ang7}* (1.42 ± 0.04), and *Elav-Gal4>UAS-GFP-Hiw; synj1$^{1/2}$* (1.14 ± 0.04). At least 8 VNCs of each genotype were used for the quantification. The error bar represents the standard error of the mean (SEM); the statistical analysis was done using one-way ANOVA followed by post hoc Tukey's test. **p<0.01, ***p<0.001; ns, not significant.

(**H-N''**) Confocal images of muscle 6/7 NMJ at A2 hemisegment showing synaptic growth in control (H-H''), *wnd$^{2/3}$* (I-I''), *AP2σ-^{KG02457}/AP2σ^{ang7}* (J-J''), *Elav-Gal4>UAS-AP2σ, AP2σ-^{KG02457}/AP2σ^{ang7}* (K-K''), *synj1$^{1/2}$* (L-L''), *wnd$^{2/3}$, AP2σ-^{KG02457}/AP2σ^{ang7}* (M-M''), and *synj1$^{1/2}$*; *wnd$^{2/3}$* (N-N'') immunolabeled for CSP (magenta) and HRP (green). The scale bar in N'' represents 10 µm.

(**O**) Histogram showing average bouton number from muscle 6/7 NMJ at A2 hemisegment for control (1.53 ± 0.07), *wnd$^{2/3}$* (0.88 ± 0.04), *AP2σ-^{KG02457}/AP2σ^{ang7}* (2.31 ± 0.13), *Elav-Gal4>UAS-AP2σ, AP2σ-^{KG02457}/AP2σ^{ang7}* (1.68 ± 0.14), *synj1$^{1/2}$* (2.46 ± 0.20), *wnd$^{2/3}$, AP2σ-^{KG02457}/AP2σ^{ang7}* (1.76 ± 0.13) and *synj1$^{1/2}$*; *wnd$^{2/3}$* (2.15 ± 0.21). At least 8 NMJs of each genotype were used for the quantifications.

(**P**) Histogram showing the average bouton area from muscle 6/7 NMJ at A2 hemisegment for control (6.56 ± 0.39), *wnd$^{2/3}$* (10.6 ± 0.59), *AP2σ-^{KG02457}/AP2σ^{ang7}* (1.16 ± 0.17), *Elav-*

Gal4>UAS-AP2σ, AP2σ-^{KG02457}/AP2σ^{ang7} (5.83 ± 0.23), *synj1$^{1/2}$* (1.31 ± 0.12), *wnd$^{2/3}$, AP2σ-^{KG02457}/AP2σ^{ang7}* (4.39 ± 0.47) and *synj1$^{1/2}$*; *wnd$^{2/3}$* (3.73 ± 0.28). At least 8 NMJs of each genotype were used for the quantifications. The error bar in O and P represents the standard error of the mean (SEM); the statistical analysis was done using one-way ANOVA followed by post hoc Tukey's test. ***p<0.001; **p<0.01; *p<0.05.

Figure 5: Endocytosis restricts hyperactivation of JNK signaling

(**A**) Schematic illustration of the JNK signaling pathway in *Drosophila.* Autophagy selectively degrades Hiw, leading to elevated levels of MAP3K Wallenda, eventually resulting in Fos and Jun (AP-1) phosphorylation. Phosphorylation of AP-1 results in activation of JNK signaling. TRE-DsRed (TRE is a synthetic promoter containing AP-1 binding sites) and puc-LacZ (puckered is a target gene of JNK signaling) were used as reporters to analyze the activation of the JNK signaling pathway.

(**B-E''**) Confocal images of third instar larval ventral nerve cord co-labelled for β-Gal (magenta) and Elav (green) in control (*puc-LacZ/+*) (B-B''), *puc-LacZ, AP2σ-^{KG02457}/AP2σ^{ang7}* (C-C''), *Elav-Gal4>UAS-AP2σ; puc-LacZ; AP2σ-^{KG02457}/AP2σ^{ang7}*, (D-D'') and *synj1$^{1/2}$; puc-LacZ/+* (E-E''). The scale bar in E'' represents 20 µm.

(**F**) Histogram showing the β-Gal levels in the third instar larval ventral nerve cord in control (*puc-LacZ/+*) (0.59 ± 0.02), *puc-LacZ, AP2σ-^{KG02457}/AP2σ^{ang7}* (1.24 ± 0.06), *Elav-Gal4>UAS-AP2σ; puc-LacZ; AP2σ-^{KG02457}/AP2σ^{ang7}* (0.48 ± 0.02), and *synj1$^{1/2}$; puc-LacZ/+* (1.43 ± 0.07). At least 9 VNCs of each genotype were used for the quantification.

(**G**) Histogram showing the β-Gal levels in the individual neuronal nuclei in control (*puc-LacZ/+*) (0.99 ± 0.09), *puc-LacZ, AP2σ-^{KG02457}/AP2σ^{ang7}* (5.92 ± 0.37), *Elav-Gal4>UAS-AP2σ; puc-LacZ; AP2σ-^{KG02457}/AP2σ^{ang7}* (1.14 ± 0.16), and *synj1$^{1/2}$; puc-LacZ/+* (5.69 ± 0.36). At least 27 nuclei of each genotype were used for the quantification. The error bar in G and H represents

the standard error of the mean (SEM); the statistical analysis was done using one-way ANOVA followed by post hoc Tukey's test. ***p<0.001; ns: not significant.

(**H-K''**) Confocal images of third instar larval ventral nerve cord co-labelled for TRE-DsRed (magenta) and Elav (green) in control (*TRE-DsRed/+*), *TRE-DsRed/+; AP2σ-^{KG02457}/AP2σ^{ang7}* (H-H''), *Elav-Gal4> UAS-AP2σ; TRE-DsRed/+; AP2σ-^{KG02457}/AP2σ^{ang7}* (I-I''), and *TRE-DsRed/+, synj1$^{1/2}$* (K-K''). The scale bar in K'' represents 20 µm.

(**L**) Histogram showing the TRE-DsRed levels in the third instar larval ventral nerve cord in control (*TRE-DsRed/+*) (1.09 ± 0.08), *TRE-DsRed/+; AP2σ-^{KG02457}/AP2σ^{ang7}* (2.17 ± 0.18), *Elav-Gal4> UAS-AP2σ; TRE-DsRed/+; AP2σ-^{KG02457}/AP2σ^{ang7}* (0.98 ± 0.08), and *TRE-DsRed/+, synj1$^{1/2}$* (1.80 ± 0.21). At least 9 VNCs of each genotype were used for the quantification.

(**M**) Histogram showing the TRE-DsRed levels in individual neuronal nuclei in control (*TRE-DsRed/+*) (2.19 ± 0.18), *TRE-DsRed/+; AP2σ-^{KG02457}/AP2σ^{ang7}* (3.56 ± 0.43), *Elav-Gal4> UAS-AP2σ; TRE-DsRed/+; AP2σ-^{KG02457}/AP2σ^{ang7}* (1.18 ± 0.13), and *TRE-DsRed, synj1$^{1/2}$* (3.34 ± 0.26). At least 47 nuclei of each genotype were used for the quantification. The error bar represents the standard error of the mean (SEM); the statistical analysis was done using one-way ANOVA followed by post hoc Tukey's test. ***p<0.001; *p<0.05; ns, not significant.

Figure 6: Elevated BMP and JNK signaling together promote synaptic overgrowth in endocytic mutants

(**A-H''**) Confocal images of muscle 6/7 NMJ at A2 hemisegment showing synaptic growth in control (A-A''), *AP2σ-^{KG02457}/AP2σ^{ang7}* (B-B''), *Elav-Gal4>UAS-AP2σ, AP2σ-^{KG02457}/AP2σ^{ang7}* (C-C''), *Elav>UAS-kay^{DN}* (D-D''), *Elav-Gal4>UAS-bsk^{DN}; AP2σ-^{KG02457}/AP2σ^{ang7}* (E-E''), *Elav-Gal4>UAS-kay^{DN}; AP2σ-^{KG02457}/AP2σ^{ang7}* (F-F''), *tkv^{7}/+; AP2σ-^{KG02457}/AP2σ^{ang7}* (G-G''), *Elav-Gal4>UAS-kay^{DN},tkv^{7}; AP2σ-^{KG02457}/AP2σ^{ang7}* (H-H'') immunolabeled for synaptic

vesicle marker CSP (magenta) and neuronal membrane marker HRP (green). The scale bar in H'' represents 10 µm.

(**I**) Histogram showing average bouton number from muscle 6/7 NMJ at A2 hemisegment in in control (w^{1118}) (1.25 ± 0.10), *AP2σ-*^{KG02457}*/AP2σ*^{ang7} (4.0 ± 0.37), *Elav-Gal4>UAS-AP2σ, AP2σ-*^{KG02457}*/AP2σ*^{ang7} (1.61 ± 0.34), *Elav>UAS-kay*^{DN} (0.98 ± 0.06), *Elav-Gal4>UAS-bsk*^{DN}*; AP2σ-*^{KG02457}*/AP2σ*^{ang7} (2.62 ± 1.83), *Elav-Gal4>UAS-kay*^{DN}*; AP2σ-*^{KG02457}*/AP2σ*^{ang7} (2.21 ± 0.21), *tkv*^{7}*/+; AP2σ-*^{KG02457}*/AP2σ*^{ang7} (2.26 ± 0.10), *Elav-Gal4>UAS-kay*^{DN}*,tkv*^{7}*; AP2σ-*^{KG02457}*/AP2σ*^{ang7} (1.88 ± 0.25). At least 9 NMJs of each genotype were used for the quantifications. The error bar represents the standard error of the mean (SEM); the statistical analysis was done using one-way ANOVA followed by post hoc Tukey's test. ***p<0.001; **p<0.01; ns, not significant.

(**J**) Histogram showing the average bouton area from muscle 6/7 NMJ at A2 hemisegment for control (8.75 ± 0.45), *AP2σ-*^{KG02457}*/AP2σ*^{ang7} (1.50 ± 0.18), *Elav-Gal4>UAS-AP2σ, AP2σ-*^{KG02457}*/AP2σ*^{ang7} (7.81 ± 0.42), *Elav>UAS-kay*^{DN} (7.70 ± 0.28), *Elav-Gal4>UAS-bsk*^{DN}*; AP2σ-*^{KG02457}*/AP2σ*^{ang7} (6.80 ± 0.50), *Elav-Gal4>UAS-kay*^{DN}*; AP2σ-*^{KG02457}*/AP2σ*^{ang7} (7.78 ± 0.65), *tkv*^{7}*/+; AP2σ-*^{KG02457}*/AP2σ*^{ang7} (5.48 ± 0.42), *Elav-Gal4>UAS-kay*^{DN}*,tkv*^{7}*; AP2σ-*^{KG02457}*/AP2σ*^{ang7} (8.94 ± 0.42). At least 10 NMJs of each genotype were used for the quantifications. The error bar represents the standard error of the mean (SEM); the statistical analysis was done using one-way ANOVA followed by post hoc Tukey's test. ***p<0.001; *p<0.05; ns, not significant.

Figure 7: Loss of Rab11 induces Highwire accumulation and liquid-liquid phase-separation in neuronal cell body

(**A-D**) Confocal images of the neuronal cell body labelled for GFP-Hiw (green) in control (*Elav-Gal4>UAS-GFP-Hiw*) (A), *Elav-Gal4>UAS-GFP-Hiw; UAS-Rab5*^{DN} (B), *Elav-*

Gal4>UAS-GFP-Hiw; UAS-Rab7^{DN} (C), and *Elav-Gal4>UAS-GFP-Hiw; UAS-Rab11^{DN}* (D). The scale bar in D represents 5 µm.

(**E**) Histogram showing the number of GFP-Hiw puncta in control (*Elav-Gal4>UAS-GFP-Hiw*) (797 ± 20.1), *Elav-Gal4>UAS-GFP-Hiw; UAS-Rab5^{DN}* (755 ± 27.4), *Elav-Gal4>UAS-GFP-Hiw; UAS-Rab7^{DN}* (709 ± 24.8), *Elav-Gal4>UAS-GFP-Hiw; UAS-Rab11^{DN}* (291 ± 22.5). At least 8 VNCs of each genotype were used for the quantification. The error bar represents the standard error of the mean (SEM); the statistical analysis was done using one-way ANOVA followed by post hoc Tukey's test. ***p<0.001, ns: not significant

(**F-G'**) Confocal images of the neuronal cell body co-labelled for GFP-Hiw (green) and Elav (magenta) in control (*Elav-Gal4>UAS-GFP-Hiw*) (F-F'), and *Elav-Gal4>UAS-GFP-Hiw; Rab11$^{ex2/93Bi}$* (G-G'). The scale bar in G' represents 5 µm.

(**H**) Histograms showing the number of GFP-Hiw puncta in the neuronal cell body of control (*Elav-Gal4>UAS-GFP-Hiw*) (716.1 ± 27.14), and *Elav-Gal4>UAS-GFP-Hiw; Rab11$^{ex2/93Bi}$* (160.5 ± 5.49). At least 12 VNCs of each genotype were used for the quantification. The error bar represents the standard error of the mean (SEM); the statistical analysis was done using Student's t-test. ***p<0.001.

(**I**) Histogram showing the average size of the GFP-Hiw puncta in the neuronal cell body of control (*Elav-Gal4>UAS-GFP-Hiw*) (0.11 ± 0.01) and *Elav-Gal4>UAS-GFP-Hiw; Rab11$^{ex2/93Bi}$* (0.28 ± 0.01). At least 12 VNCs of each genotype were used for the quantification. The error bar represents the standard error of the mean (SEM); the statistical analysis was done using Student's t-test. ***p<0.001.

(**J**) Western blot showing the level of GFP-Hiw in control (*Elav-Gal4>UAS-GFP-Hiw*) and *Elav-Gal4>UAS-GFP-Hiw; Rab11$^{ex2/93Bi}$*. Ran was used as a loading control.

(**K**) Histogram showing the level of GFP-Hiw in control (*Elav-Gal4>UAS-GFP-Hiw*) (1.00 ± 0.00) and *Elav-Gal4>UAS-GFP-Hiw; Rab11$^{ex2/93Bi}$* (1.67 ± 0.05). Three independent Western

blots were used for quantification. The error bar represents the standard error of the mean (SEM); the statistical analysis was done using Student's t-test. ***p<0.001.

(**L-N''**) Confocal images of third instar larval ventral nerve cord co-labelled for Wnd (magenta) and NC82 (green) in control (L-L''), *Rab11*$^{ex2/93Bi}$ (M-M''), and *AP2σ*-^{KG02457}/*AP2σ*^{ang7} (N-N''). The scale bar in N'' represents 10 µm.

(**O**) Histogram showing the average fluorescence intensity of Wnd in control (0.55 ± 0.02), *Rab11*$^{ex2/93Bi}$ (0.84 ± 0.03), and *AP2σ*-^{KG02457}/*AP2σ*^{ang7} (1.03 ± 0.05). At least 10 VNCs of each genotype were used for the quantification. The error bar represents the standard error of the mean (SEM); the statistical analysis was done using one-way ANOVA followed by post hoc Tukey's test. ***p<0.001.

Figure 8: Endocytosis restricts JNK and BMP signaling through Rab11 in a parallel pathway

(**A-D''**) Confocal images of muscle 6/7 NMJ showing the synaptic growth in control (A-A''), *Rab11*$^{ex2/93Bi}$ (B-B''), *Elav-Gal4>UAS-bsk*^{DN}; *Rab11*$^{ex2/93Bi}$ (C-C''), and *Elav-Gal4>UAS-kay*^{DN}; *Rab11*$^{ex2/93Bi}$ (D-D'') immunolabeled for CSP (magenta) and HRP (green). The scale bar in D'' represents 10 µm.

(**E**) Histogram showing average bouton number from muscle 6/7 NMJ at A2 hemisegment in control (1.40 ± 0.07), *Rab11*$^{ex2/93Bi}$ (3.70 ± 0.07), *Elav-Gal4>UAS- bsk*^{DN}; *Rab11*$^{ex2/93Bi}$ (1.53 ± 0.0) and *Elav-Gal4>UAS-kay*^{DN}; *Rab11*$^{ex2/93Bi}$ (1.64 ± 0.117). At least 8 NMJs of each genotype were used for the quantifications. The error bar represents the standard error of the mean (SEM); the statistical analysis was done using one-way ANOVA followed by post hoc Tukey's test. ***p<0.001; **p<0.01; *p<0.05

(**F**) Histogram showing the average bouton area from muscle 6/7 NMJ at A2 hemisegment in control (5.87 ± 0.87), *Rab11*$^{ex2/93Bi}$ (2.02 ± 0.19), *Elav-Gal4>UAS-bsk*^{DN}; *Rab11*$^{ex2/93Bi}$ (7.33 ±

0.88), and *Elav-Gal4>UAS-kay*^{DN}*; Rab11*$^{ex2/93Bi}$ (6.91 ± 0.21). At least 8 NMJs of each genotype were used for the quantifications. The error bar represents the standard error of the mean (SEM); the statistical analysis was done using one-way ANOVA followed by post hoc Tukey's test. **p<0.01; ns, not significant.

(G) A proposed model for the regulation of synaptic growth signaling. Endocytosis regulates Rab11-positive recycling endosomes, which in turn modulate three partially independent pathways to attenuate synaptic growth. First, Rab11 regulates endosomal trafficking of Hiw; when trafficking is impaired, Hiw undergoes phase separation into large non-functional assemblies, which hyperactivates JNK signaling. Second, reduced Rab11 compromises autophagosome formation and autophagy, leading to elevated Hiw levels, which accumulate as phase-separated condensates in the endocytic mutants. Third, Rab11 regulates BMP receptor trafficking, and its reduction leads to increased pMad levels. These pathways suggest that endocytosis restricts synaptic growth by restraining BMP and JNK signaling in a parallel pathway mediated by Rab11-dependent endosomal trafficking, with Hiw phase separation as a key regulatory mechanism.

References

Abrams, B., B. Grill, X. Huang and Y. Jin, 2008 Cellular and molecular determinants targeting the Caenorhabditis elegans PHR protein RPM-1 to perisynaptic regions. Dev Dyn 237: 630-639.

Agnes, F., M. Suzanne and S. Noselli, 1999 The Drosophila JNK pathway controls the morphogenesis of imaginal discs during metamorphosis. Development 126: 5453-5462.

Andres-Alonso, M., M. R. Kreutz and A. Karpova, 2021 Autophagy and the endolysosomal system in presynaptic function. Cell Mol Life Sci 78: 2621-2639.

Bakthavachalu, B., J. Huelsmeier, I. P. Sudhakaran, J. Hillebrand, A. Singh *et al.*, 2018 RNP-Granule Assembly via Ataxin-2 Disordered Domains Is Required for Long-Term Memory and Neurodegeneration. Neuron 98**:** 754-766 e754.

Ball, R. W., M. Warren-Paquin, K. Tsurudome, E. H. Liao, F. Elazzouzi *et al.*, 2010 Retrograde BMP Signaling Controls Synaptic Growth at the NMJ by Regulating Trio Expression in Motor Neurons. Neuron 66**:** 536-549.

Bartz, R., C. Benzing and O. Ullrich, 2003 Reconstitution of vesicular transport to Rab11-positive recycling endosomes in vitro. Biochemical and Biophysical Research Communications 312**:** 663-669.

Bastrikova, N., G. A. Gardner, J. M. Reece, A. Jeromin and S. M. Dudek, 2008 Synapse elimination accompanies functional plasticity in hippocampal neurons. Proc Natl Acad Sci U S A 105**:** 3123-3127.

Becker, L. A., B. Huang, G. Bieri, R. Ma, D. A. Knowles *et al.*, 2017 Therapeutic reduction of ataxin-2 extends lifespan and reduces pathology in TDP-43 mice. Nature 544**:** 367-371.

Bera, S., S. Camblor-Perujo, E. C. Barca, A. Negrete-Hurtado, J. Racho *et al.*, 2020 AP-2 reduces amyloidogenesis by promoting BACE1 trafficking and degradation in neurons. Embo Reports 21.

Bharmauria, V., A. Ouelhazi, R. Lussiez and S. Molotchnikoff, 2022 Adaptation-induced plasticity in the sensory cortex. J Neurophysiol 128**:** 946-962.

Birgisdottir, A. B., and T. Johansen, 2020 Autophagy and endocytosis - interconnections and interdependencies. Journal of Cell Science 133.

Chatterjee, N., and D. Bohmann, 2012 A versatile PhiC31 based reporter system for measuring AP-1 and Nrf2 signaling in Drosophila and in tissue culture. PLoS One 7**:** e34063.

Chou, V. T., S. A. Johnson and D. Van Vactor, 2020 Synapse development and maturation at the neuromuscular junction. Neural Development 15.

Choudhury, S. D., M. K. Dwivedi, S. Pippadpally, A. Patnaik, S. Mishra *et al.*, 2022 AP2 Regulates Thickveins Trafficking to Attenuate NMJ Growth Signaling in Drosophila. eNeuro 9.

Choudhury, S. D., Z. Mushtaq, S. Reddy-Alla, S. S. Balakrishnan, R. S. Thakur *et al.*, 2016 sigma2-Adaptin Facilitates Basal Synaptic Transmission and Is Required for Regenerating Endo-Exo Cycling Pool Under High-Frequency Nerve Stimulation in Drosophila. Genetics 203**:** 369-385.

Collins, C. A., and A. DiAntonio, 2007a Synaptic development: insights from Drosophila. Curr Opin Neurobiol 17**:** 35-42.

Collins, C. A., and A. DiAntonio, 2007b Synaptic development:: insights from. Current Opinion in Neurobiology 17**:** 35-42.

Collins, C. A., Y. P. Wairkar, S. L. Johnson and A. DiAntonio, 2006 Highwire restrains synaptic growth by attenuating a MAP kinase signal. Neuron 51**:** 57-69.

Colon-Ramos, D. A., 2009 Synapse formation in developing neural circuits. Curr Top Dev Biol 87**:** 53-79.

Cosker, K. E., and R. A. Segal, 2014 Neuronal signaling through endocytosis. Cold Spring Harb Perspect Biol 6.

Craven, S. E., and D. S. Bredt, 1998 PDZ proteins organize synaptic signaling pathways. Cell 93**:** 495-498.

Dejanovic, B., M. Sheng and J. E. Hanson, 2024 Targeting synapse function and loss for treatment of neurodegenerative diseases. Nat Rev Drug Discov 23**:** 23-42.

Deshpande, M., and A. A. Rodal, 2016 The Crossroads of Synaptic Growth Signaling, Membrane Traffic and Neurological Disease: Insights from Drosophila. Traffic 17**:** 87-101.

DeVorkin, L., and S. M. Gorski, 2014 Monitoring autophagy in Drosophila using fluorescent reporters in the UAS-GAL4 system. Cold Spring Harb Protoc 2014**:** 967-972.

Di Fiore, P. P., and P. De Camilli, 2001 Endocytosis and signaling. an inseparable partnership. Cell 106**:** 1-4.

Dickman, D. K., Z. Lu, I. A. Meinertzhagen and T. L. Schwarz, 2006 Altered synaptic development and active zone spacing in endocytosis mutants. Curr Biol 16**:** 591-598.
Ehrlich, M., 2016 Endocytosis and trafficking of BMP receptors: Regulatory mechanisms for fine-tuning the signaling response in different cellular contexts. Cytokine & Growth Factor Reviews 27**:** 35-42.
Gleason, R. J., A. M. Akintobi, B. D. Grant and R. W. Padgett, 2014 BMP signaling requires retromer-dependent recycling of the type I receptor. Proceedings of the National Academy of Sciences of the United States of America 111**:** 2578-2583.
Gleason, R. J., M. Vora, Y. Li, N. S. Kane, K. Liao *et al.*, 2017 SMA-10 regulates BMP receptor trafficking. Plos One 12.
Goold, C. P., and G. W. Davis, 2007 The BMP ligand Gbb gates the expression of synaptic homeostasis independent of synaptic growth control. Neuron 56**:** 109-123.
Green, E. G., E. Ramm, N. M. Riley, D. J. Spiro, J. R. Goldenring *et al.*, 1997 Rab11 is associated with transferrin-containing recycling compartments in K562 cells. Biochemical and Biophysical Research Communications 239**:** 612-616.
Grill, B., W. V. Bienvenut, H. M. Brown, B. D. Ackley, M. Quadroni *et al.*, 2007 RPM-1 regulates axon termination and synaptogenesis through the Rab GEF GLO-4 and the Rab GTPase GLO-1. Neuron 55**:** 587-601.
Hedrick, N. G., W. J. Wright and T. Komiyama, 2024 Local and global predictors of synapse elimination during motor learning. Sci Adv 10**:** eadk0540.
Heerssen, H., R. D. Fetter and G. W. Davis, 2008 Clathrin dependence of synaptic-vesicle formation at the Drosophila neuromuscular junction. Curr Biol 18**:** 401-409.
Hernandez-Diaz, S., S. Ghimire, I. Sanchez-Mirasierra, C. Montecinos-Oliva, J. Swerts *et al.*, 2022 Endophilin-B regulates autophagy during synapse development and neurodegeneration. Neurobiology of Disease 163.
Hoffmann-Conaway, S., M. M. Brockmann, K. Schneider, A. Annamneedi, K. A. Rahman *et al.*, 2020 Parkin contributes to synaptic vesicle autophagy in Bassoon-deficient mice. Elife 9.
Jacomin, A. C., A. Bescond, E. Soleilhac, B. Gallet, G. Schoehn *et al.*, 2015 The Deubiquitinating Enzyme UBPY Is Required for Lysosomal Biogenesis and Productive Autophagy in. Plos One 10.
Jiang, X., R. Sando and T. C. Sudhof, 2021 Multiple signaling pathways are essential for synapse formation induced by synaptic adhesion molecules. Proc Natl Acad Sci U S A 118.
Kakuta, S., J. Yamaguchi, C. Suzuki, M. Sasaki, S. Kazuno *et al.*, 2017 Small GTPase Rab1B is associated with ATG9A vesicles and regulates autophagosome formation. Faseb Journal 31**:** 3757-3773.
Keshishian, H., and Y. S. Kim, 2004 Orchestrating development and function: retrograde BMP signaling in the Drosophila nervous system. Trends Neurosci 27**:** 143-147.
Khodosh, R., A. Augsburger, T. L. Schwarz and P. A. Garrity, 2006 Bchs, a BEACH domain protein, antagonizes Rab11 in synapse morphogenesis and other developmental events. Development 133**:** 4655-4665.
Kim, S. M., Y. Quagraine, M. Singh and J. H. Kim, 2024 Rab11 suppresses neuronal stress signaling by localizing dual leucine zipper kinase to axon terminals for protein turnover. Elife 13.
Kononenko, N. L., G. A. Classen, M. Kuijpers, D. Puchkov, T. Maritzen *et al.*, 2017 Retrograde transport of TrkB-containing autophagosomes via the adaptor AP-2 mediates neuronal complexity and prevents neurodegeneration. Nat Commun 8**:** 14819.
Kosaka, T., and K. Ikeda, 1983 Reversible blockage of membrane retrieval and endocytosis in the garland cell of the temperature-sensitive mutant of Drosophila melanogaster, shibirets1. J Cell Biol 97**:** 499-507.
Kroll, J. R., K. G. Wong, F. M. Siddiqui and M. A. Tanouye, 2015 Disruption of Endocytosis with the Dynamin Mutant shibirets1 Suppresses Seizures in Drosophila. Genetics 201**:** 1087-1102.
Kroschwald, S., S. Maharana and A. W. Simon, 2017 Hexanediol: a chemical probe to investigate the material properties of membrane-less compartments, pp.

Lancaster, A. K., A. Nutter-Upham, S. Lindquist and O. D. King, 2014 PLAAC: a web and command-line application to identify proteins with prion-like amino acid composition. Bioinformatics 30**:** 2501-2502.

Laugks, U., M. Hieke and N. Wagner, 2017 MAN1 Restricts BMP Signaling During Synaptic Growth in Drosophila. Cell Mol Neurobiol 37**:** 1077-1093.

Leitch, C. C., S. Lodh, V. Prieto-Echague, J. L. Badano and N. A. Zaghloul, 2014 Basal body proteins regulate Notch signaling through endosomal trafficking. J Cell Sci 127**:** 2407-2419.

Liu, Z., Y. Yang, A. Gu, J. Xu, Y. Mao *et al.*, 2020 Par complex cluster formation mediated by phase separation. Nat Commun 11**:** 2266.

Longatti, A., C. A. Lamb, M. Razi, S. Yoshimura, F. A. Barr *et al.*, 2012 TBC1D14 regulates autophagosome formation via Rab11-and ULK1-positive recycling endosomes. Journal of Cell Biology 197**:** 659-675.

Longatti, A., and S. A. Tooze, 2012 Recycling endosomes contribute to autophagosome formation. Autophagy 8**:** 1682-1683.

Low, P., A. Varga, K. Pircs, P. Nagy, Z. Szatmári *et al.*, 2013 Impaired proteasomal degradation enhances autophagy via hypoxia signaling in Drosophila. Bmc Cell Biology 14.

Martín-Blanco, E., A. Gampel, J. Ring, K. Virdee, N. Kirov *et al.*, 1998 puckered encodes a phosphatase that mediates a feedback loop regulating JNK activity during dorsal closure in Drosophila. Genes & Development 12**:** 557-570.

Mauvezin, C., C. Ayala, C. R. Braden, J. Kim and T. P. Neufeld, 2014 Assays to monitor autophagy in Drosophila. Methods 68**:** 134-139.

Mauvezin, C., P. Nagy, G. Juhasz and T. P. Neufeld, 2015 Autophagosome-lysosome fusion is independent of V-ATPase-mediated acidification. Nat Commun 6**:** 7007.

McCabe, B. D., S. Hom, H. Aberle, R. D. Fetter, G. Marques *et al.*, 2004 Highwire regulates presynaptic BMP signaling essential for synaptic growth. Neuron 41**:** 891-905.

McCabe, B. D., G. Marqués, A. P. Haghighi, R. D. Fetter, M. L. Crotty *et al.*, 2003 The BMP homolog Gbb provides a retrograde signal that regulates synaptic growth at the

neuromuscular junction. Neuron 39**:** 241-254.

McDonald, N. A., R. D. Fetter and K. Shen, 2020 Assembly of synaptic active zones requires phase separation of scaffold molecules. Nature 588**:** 454-458.

Meszaros, B., G. Erdos and Z. Dosztanyi, 2018 IUPred2A: context-dependent prediction of protein disorder as a function of redox state and protein binding. Nucleic Acids Res 46**:** W329-W337.

Mottola, G., A. K. Classen, M. Gonzalez-Gaitan, S. Eaton and M. Zerial, 2010 A novel function for the Rab5 effector Rabenosyn-5 in planar cell polarity. Development 137**:** 2353-2364.

Nair, S. J., L. Yang, D. Meluzzi, S. Oh, F. Yang *et al.*, 2019 Phase separation of ligand-activated enhancers licenses cooperative chromosomal enhancer assembly. Nat Struct Mol Biol 26**:** 193-203.

O'Connor-Giles, K. M., L. L. Ho and B. Ganetzky, 2008 Nervous wreck interacts with thickveins and the endocytic machinery to attenuate retrograde BMP signaling during synaptic growth. Neuron 58**:** 507-518.

Opperman, K. J., and B. Grill, 2014a RPM-1 is localized to distinct subcellular compartments and regulates axon length in GABAergic motor neurons. Neural Dev 9**:** 10.

Opperman, K. J., and B. Grill, 2014b RPM-1 is localized to distinct subcellular compartments and regulates axon length in GABAergic motor neurons. Neural Development 9.

Papoulas, O., K. F. Monzo, G. T. Cantin, C. Ruse, J. R. Yates, 3rd *et al.*, 2010 dFMRP and Caprin, translational regulators of synaptic plasticity, control the cell cycle at the Drosophila mid-blastula transition. Development 137**:** 4201-4209.

Puri, C., M. Renna, C. F. Bento, K. Moreau and D. C. Rubinsztein, 2013 Diverse Autophagosome Membrane Sources Coalesce in Recycling Endosomes. Cell 154**:** 1285-1299.

Ravikumar, B., K. Moreau, L. Jahreiss, C. Puri and D. C. Rubinsztein, 2010 Plasma membrane contributes to the formation of pre-autophagosomal structures (vol 12, pg 747, 2010). Nature Cell Biology 12**:** 1021-1021.

Ring, J. M., and A. Martinez Arias, 1993 puckered, a gene involved in position-specific cell differentiation in the dorsal epidermis of the Drosophila larva. Dev Suppl**:** 251-259.

Rodal, A. A., A. D. Blunk, Y. Akbergenova, R. A. Jorquera, L. K. Buhl *et al.*, 2011 A presynaptic endosomal trafficking pathway controls synaptic growth signaling. Journal of Cell Biology 193**:** 201-217.

Rodal, A. A., R. N. Motola-Barnes and J. T. Littleton, 2008 Nervous wreck and Cdc42 cooperate to regulate endocytic actin assembly during synaptic growth. J Neurosci 28**:** 8316-8325.

Royle, S. J., and L. Lagnado, 2003 Endocytosis at the synaptic terminal. J Physiol 553**:** 345-355.

Scott, R. C., O. Schuldiner and T. P. Neufeld, 2004 Role and regulation of starvation-induced autophagy in the Drosophila fat body. Dev Cell 7**:** 167-178.

Shen, W., and B. Ganetzky, 2009 Autophagy promotes synapse development in. Journal of Cell Biology 187**:** 71-79.

Smith, R. B., J. B. Machamer, N. C. Kim, T. S. Hays and G. Marqués, 2012 Relay of retrograde synaptogenic signals through axonal transport of BMP receptors. Journal of Cell Science 125**:** 3752-3764.

Soukup, S. F., S. Kuenen, R. Vanhauwaert, J. Manetsberger, S. Hernandez-Diaz *et al.*, 2016 A LRRK2-Dependent EndophilinA Phosphoswitch Is Critical for Macroautophagy at Presynaptic Terminals. Neuron 92**:** 829-844.

Tanaka, T., and A. Nakamura, 2008 The endocytic pathway acts downstream of Oskar in Drosophila germ plasm assembly. Development 135**:** 1107-1117.

Tian, Y., J. C. Chang, E. Y. Fan, M. Flajolet and P. Greengard, 2013 Adaptor complex AP2/PICALM, through interaction with LC3, targets Alzheimer's APP-CTF for terminal degradation via autophagy. Proc Natl Acad Sci U S A 110**:** 17071-17076.

Tooze, S. A., A. Abada and Z. Elazar, 2014 Endocytosis and autophagy: exploitation or cooperation? Cold Spring Harb Perspect Biol 6**:** a018358.

Ullrich, O., S. Reinsch, S. Urbé, M. Zerial and R. G. Parton, 1996 Rab11 regulates recycling through the pericentriolar recycling endosome. Journal of Cell Biology 135**:** 913-924.

Vanhauwaert, R., S. Kuenen, R. Masius, A. Bademosi, J. Manetsberger *et al.*, 2017 The SAC1 domain in synaptojanin is required for autophagosome maturation at presynaptic terminals. EMBO J 36**:** 1392-1411.

Vanlandingham, P. A., T. R. Fore, L. R. Chastain, S. M. Royer, H. Bao *et al.*, 2013 Epsin 1 Promotes Synaptic Growth by Enhancing BMP Signal Levels in Motoneuron Nuclei. Plos One 8.

Wan, H. I., A. DiAntonio, R. D. Fetter, K. Bergstrom, R. Strauss *et al.*, 2000 Highwire regulates synaptic growth in Drosophila. Neuron 26**:** 313-329.

Washbourne, P., 2015 Synapse assembly and neurodevelopmental disorders. Neuropsychopharmacology 40**:** 4-15.

West, R. J. H., Y. B. Lu, B. Marie, F. B. Gao and S. T. Sweeney, 2015 Rab8, POSH, and TAK1 regulate synaptic growth in a

model of frontotemporal dementia. Journal of Cell Biology 208**:** 931-947.

Wilcke, M., L. Johannes, T. Galli, V. Mayau, B. Goud *et al.*, 2000 Rab11 regulates the compartmentalization of early endosomes required for efficient transport from early endosomes to the trans-golgi network. Journal of Cell Biology 151**:** 1207-1220.

Wu, C., Y. P. Wairkar, C. A. Collins and A. DiAntonio, 2005a Highwire function at the Drosophila neuromuscular junction: spatial, structural, and temporal requirements. J Neurosci 25**:** 9557-9566.

Wu, C. L., R. W. Daniels and A. DiAntonio, 2007 DFsn collaborates with Highwire to down-regulate the Wallenda/DLK kinase and restrain synaptic terminal growth. Neural Development 2.

Wu, C. L., Y. P. Wairkar, C. A. Collins and A. DiAntonio, 2005b function at the

neuromuscular junction:: Spatial, structural, and temporal requirements. Journal of Neuroscience 25**:** 9557-9566.

Xiong, X., X. Wang, R. Ewanek, P. Bhat, A. DiAntonio *et al.*, 2010 Protein turnover of the Wallenda/DLK kinase regulates a retrograde response to axonal injury. Journal of Cell Biology 191**:** 211-223.

Yoshii, A., and M. Constantine-Paton, 2010 Post-synaptic BDNF-TrkB signaling in synapse maturation, plasticity, and disease. Dev Neurobiol 70**:** 304-322.

Zeng, M., Y. Shang, Y. Araki, T. Guo, R. L. Huganir *et al.*, 2016 Phase Transition in Post-synaptic Densities Underlies Formation of Synaptic Complexes and Synaptic Plasticity. Cell 166**:** 1163-1175 e1112.

Zhao, L., D. Wang, Q. Wang, A. A. Rodal and Y. Q. Zhang, 2013 Drosophila cyfip regulates synaptic development and endocytosis by suppressing filamentous actin assembly. PLoS Genet 9**:** e1003450.

Zhu, S. J., R. Chen, P. Soba and Y. N. Jan, 2019 JNK signaling coordinates with ecdysone signaling to promote pruning of

sensory neuron dendrites. Development 146.

Zirin, J., J. Nieuwenhuis and N. Perrimon, 2013 Role of autophagy in glycogen breakdown and its relevance to chloroquine myopathy. PLoS Biol 11**:** e1001708.

Zulkefli, K. L., F. J. Houghton, P. Gosavi and P. A. Gleeson, 2019 A role for Rab11 in the homeostasis of the endosome-lysosomal pathway. Experimental Cell Research 380**:** 55-68.

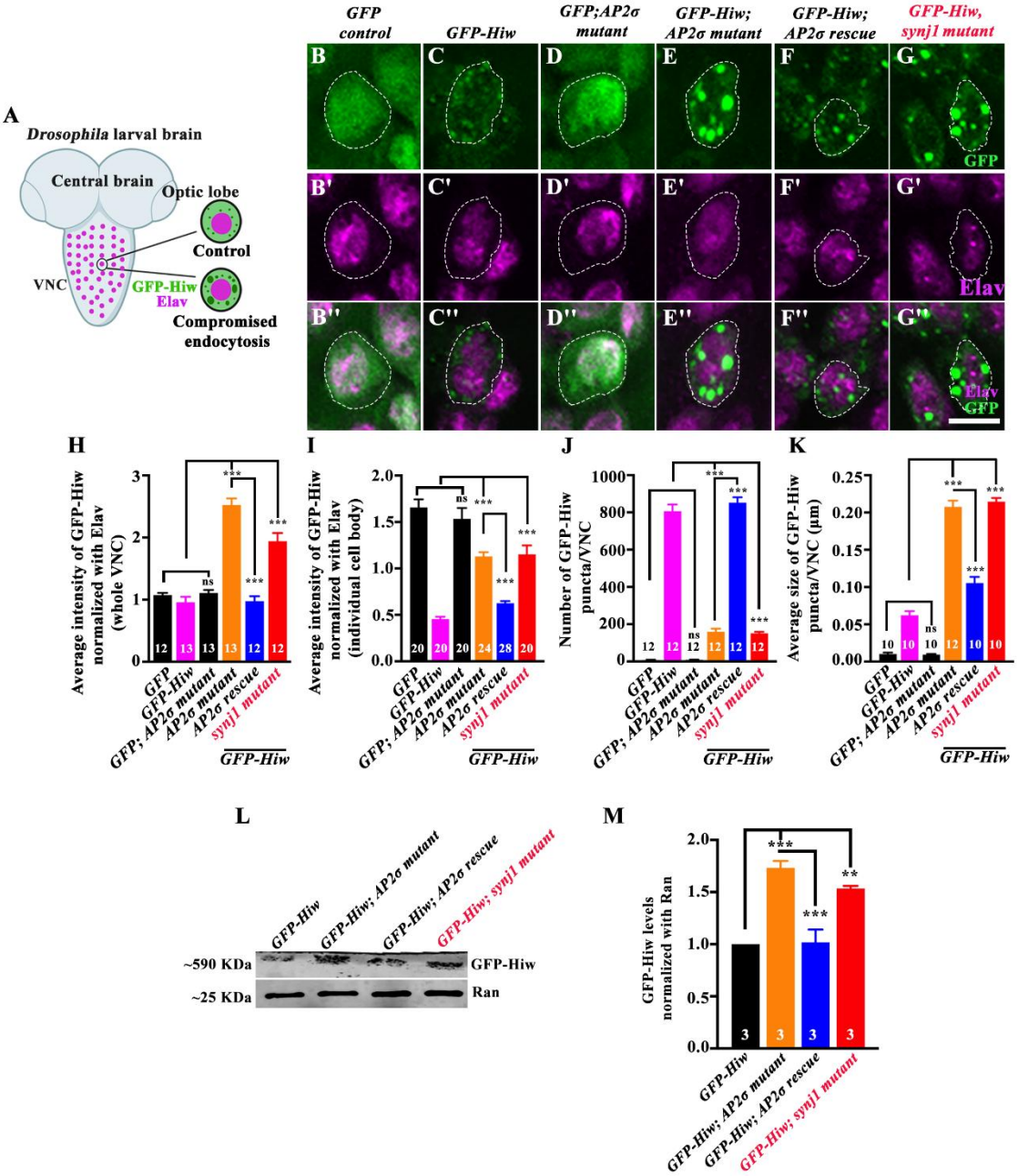
A
Drosophila larval brain
Central brain
Optic lobe
Control
VNC
GFP-Hiw
Elav
Compromised endocytosis
GFP control
GFP-Hiw
GFP;AP2σ mutant
GFP-Hiw; AP2σ mutant
GFP-Hiw; AP2σ rescue
GFP-Hiw, synj1 mutant
GFP
Elav
H
Average intensity of GFP-Hiw normalized with Elav (whole VNC)
I
Average intensity of GFP-Hiw normalized with Elav (individual cell body)
J
Number of GFP-Hiw puncta/VNC
K
Average size of GFP-Hiw puncta/VNC (μm)
GFP
GFP-Hiw
GFP; AP2σ mutant
AP2σ mutant
AP2σ rescue
synj1 mutant
GFP-Hiw
L
GFP-Hiw
GFP-Hiw; AP2σ mutant
GFP-Hiw; AP2σ rescue
GFP-Hiw; synj1 mutant
~590 KDa
~25 KDa
Ran
M
GFP-Hiw levels normalized with Ran

Figure_1

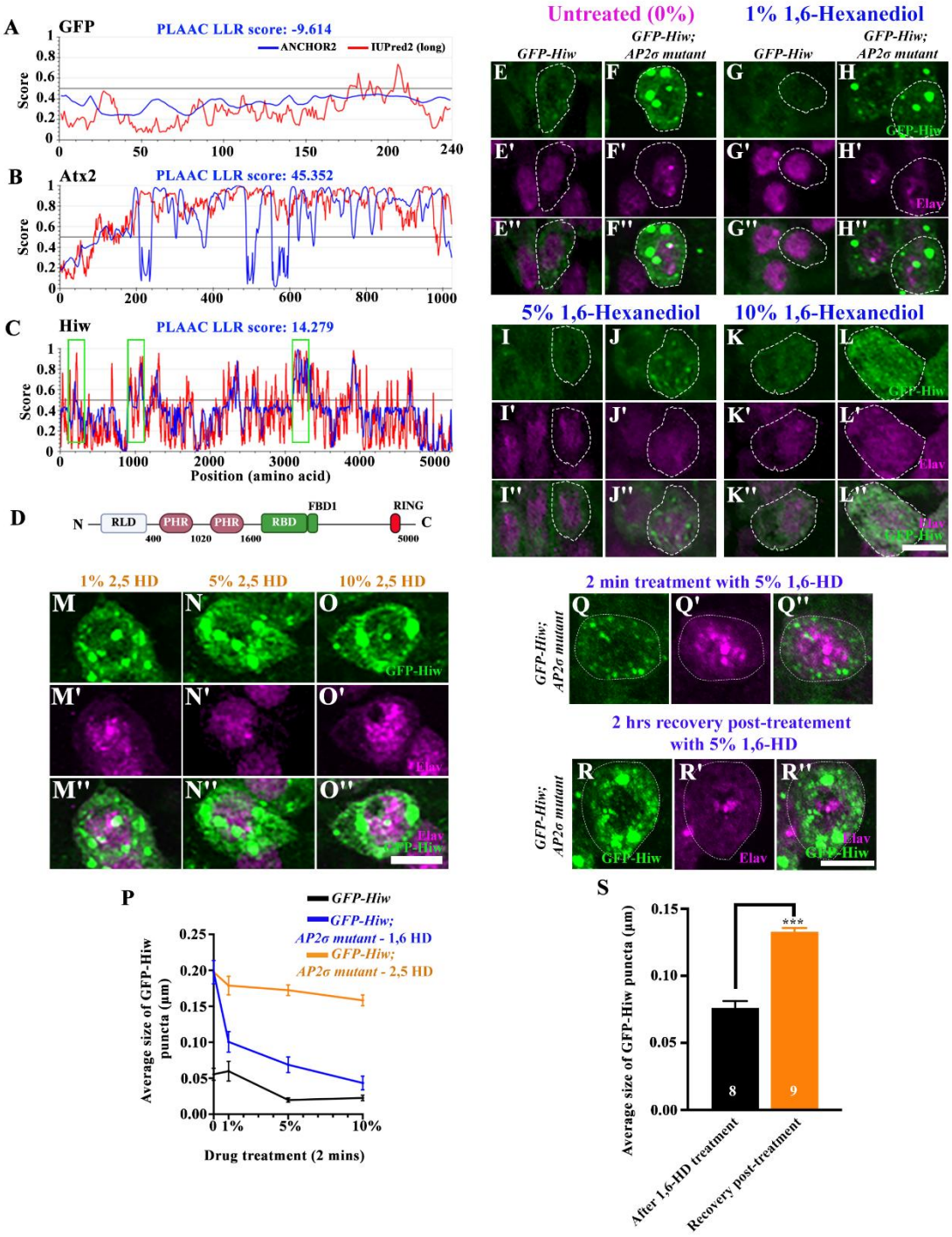
A
GFP
PLAAC LLR score: -9.614
ANCHOR2
IUPred2 (long)
Score
B
Atx2
PLAAC LLR score: 45.352
C
Hiw
PLAAC LLR score: 14.279
Position (amino acid)
D
N
RLD
PHR
PHR
RBD
FBD1
RING
C
Untreated (0%)
1% 1,6-Hexanediol
GFP-Hiw
GFP-Hiw; AP2σ mutant
5% 1,6-Hexanediol
10% 1,6-Hexanediol
1% 2,5 HD
5% 2,5 HD
10% 2,5 HD
2 min treatment with 5% 1,6-HD
2 hrs recovery post-treatement with 5% 1,6-HD
Elav
P
GFP-Hiw
GFP-Hiw; AP2σ mutant - 1,6 HD
GFP-Hiw; AP2σ mutant - 2,5 HD
Average size of GFP-Hiw puncta (µm)
Drug treatment (2 mins)
S
Average size of GFP-Hiw puncta (µm)
After 1,6-HD treatment
Recovery post-treatment

Figure_2

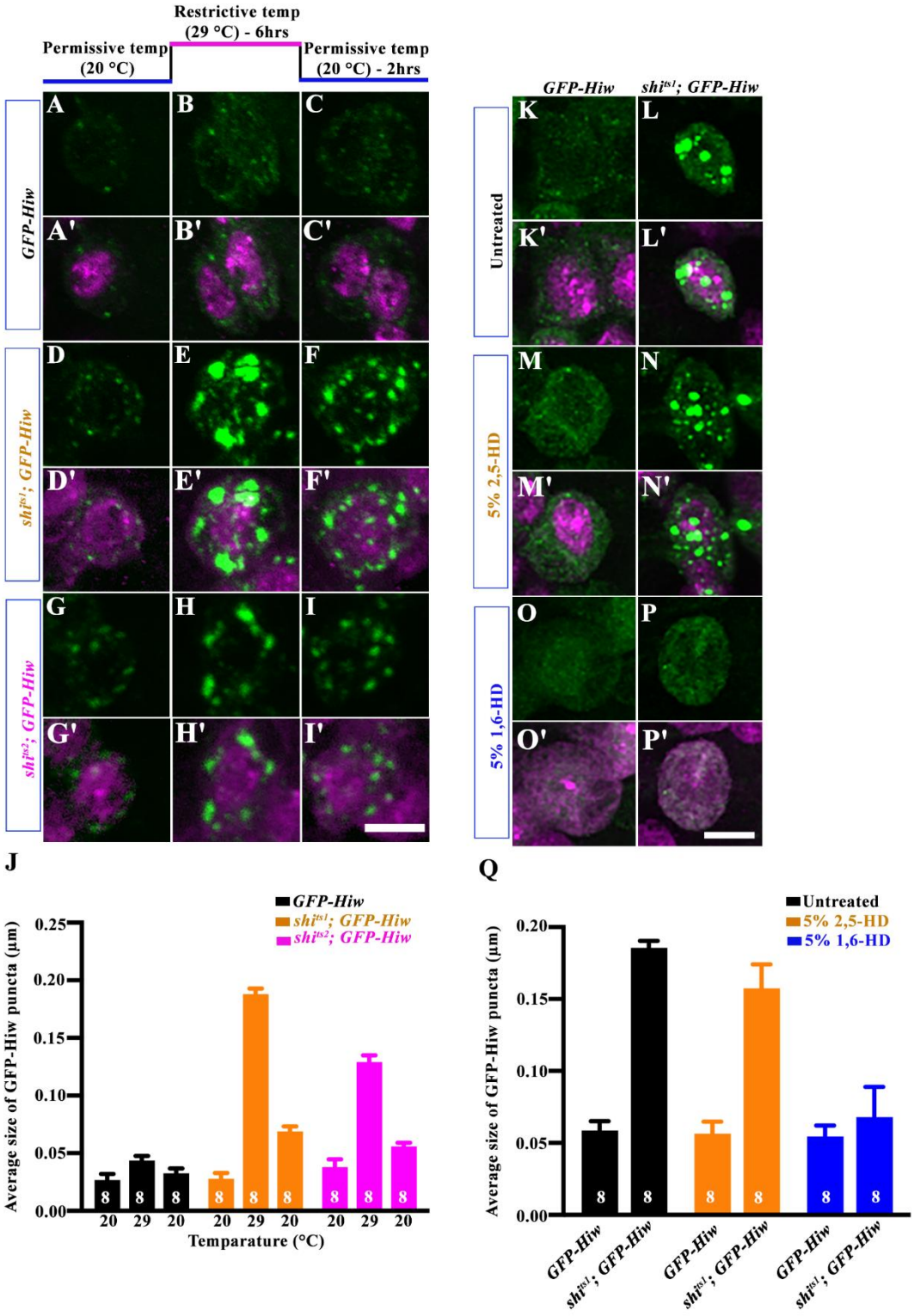
Restrictive temp
(29 °C) - 6hrs
Permissive temp
(20 °C)
Permissive temp
(20 °C) - 2hrs
GFP-Hiw
shi^ts1; GFP-Hiw
shi^ts2; GFP-Hiw
A
B
C
A'
B'
C'
D
E
F
D'
E'
F'
G
H
I
G'
H'
I'
GFP-Hiw
shi^ts1; GFP-Hiw
Untreated
5% 2,5-HD
5% 1,6-HD
K
L
K'
L'
M
N
M'
N'
O
P
O'
P'
J
GFP-Hiw
shi^ts1; GFP-Hiw
shi^ts2; GFP-Hiw
Average size of GFP-Hiw puncta (µm)
0.25
0.20
0.15
0.10
0.05
0.00
8
20 29 20 20 29 20 20 29 20
Temparature (°C)
Q
Untreated
5% 2,5-HD
5% 1,6-HD
Average size of GFP-Hiw puncta (µm)
0.20
0.15
0.10
0.05
0.00
8
GFP-Hiw
shi^ts1; GFP-Hiw
GFP-Hiw
shi^ts1; GFP-Hiw
GFP-Hiw
shi^ts1; GFP-Hiw

Figure_3

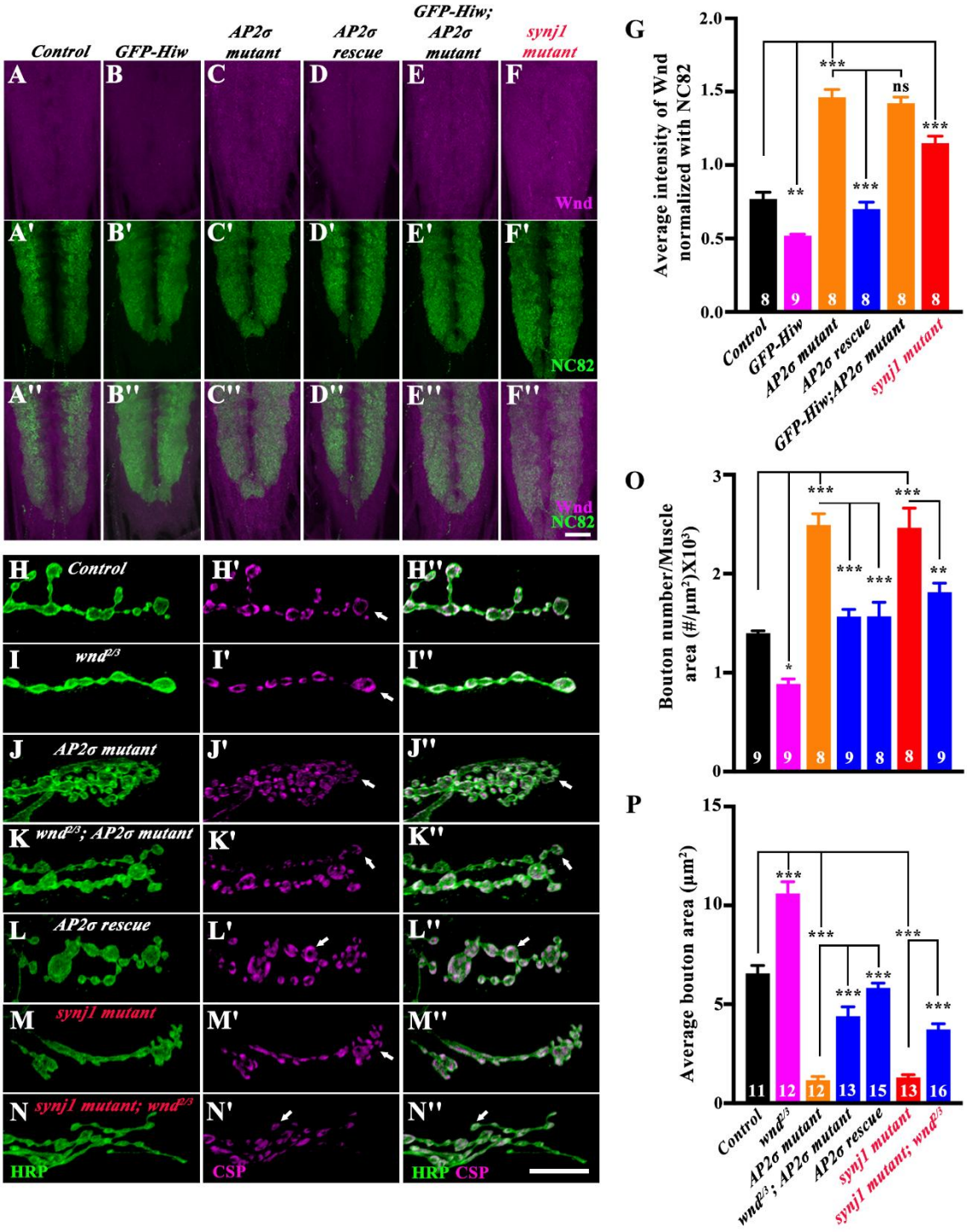
Control
GFP-Hiw
AP2σ mutant
AP2σ rescue
GFP-Hiw; AP2σ mutant
synj1 mutant
Wnd
NC82
Wnd NC82
Control
wnd2/3
AP2σ mutant
wnd2/3; AP2σ mutant
AP2σ rescue
synj1 mutant
synj1 mutant; wnd2/3
HRP
CSP
HRP CSP
G
Average intensity of Wnd normalized with NC82
O
Bouton number/Muscle area (#/μm²)X10³
P
Average bouton area (μm²)
ns

Figure_4

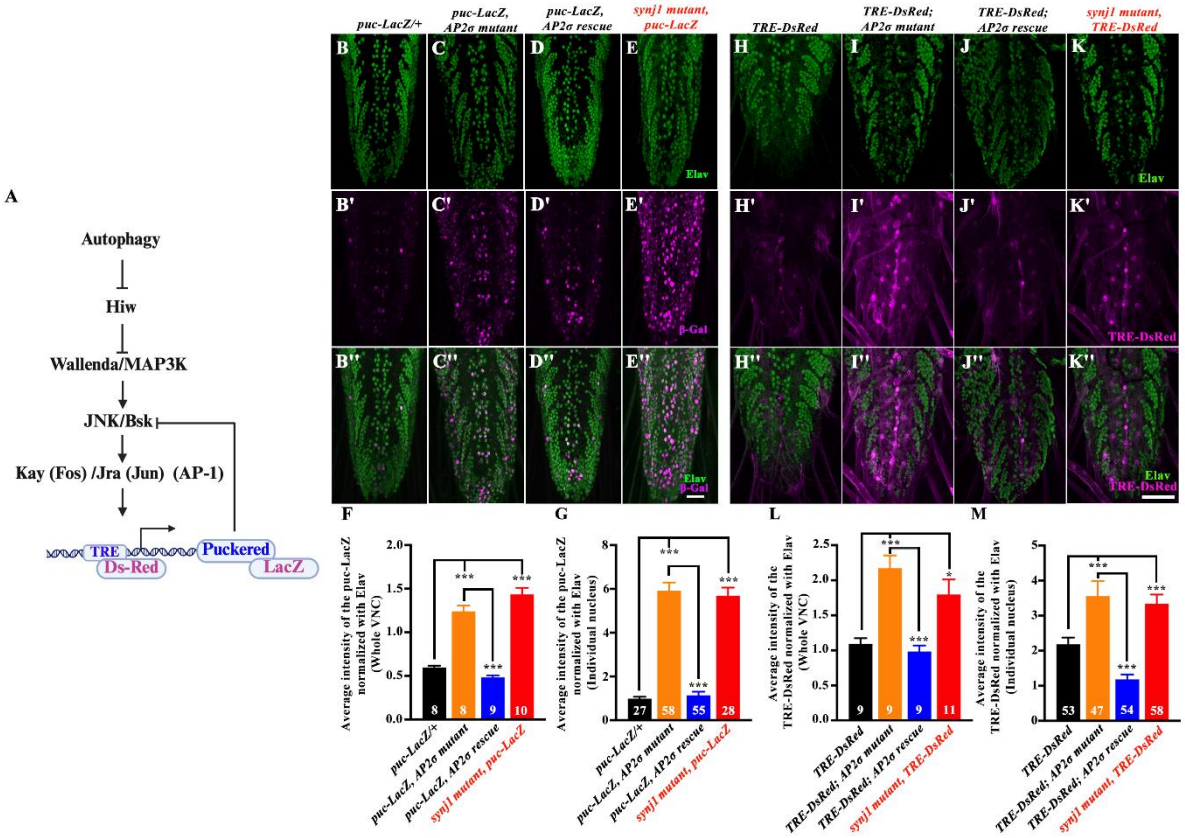
A
Autophagy
Hiw
Wallenda/MAP3K
JNK/Bsk
Kay (Fos) /Jra (Jun) (AP-1)
TRE
Ds-Red
Puckered
LacZ
puc-LacZ/+
puc-LacZ, AP2σ mutant
puc-LacZ, AP2σ rescue
synj1 mutant, puc-LacZ
TRE-DsRed
TRE-DsRed; AP2σ mutant
TRE-DsRed; AP2σ rescue
synj1 mutant, TRE-DsRed
Elav
β-Gal
TRE-DsRed
F
G
L
M
Average intensity of the puc-LacZ normalized with Elav (Whole VNC)
Average intensity of the puc-LacZ normalized with Elav (Individual nucleus)
Average intensity of the TRE-DsRed normalized with Elav (Whole VNC)
Average intensity of the TRE-DsRed normalized with Elav (Individual nucleus)

Figure_5

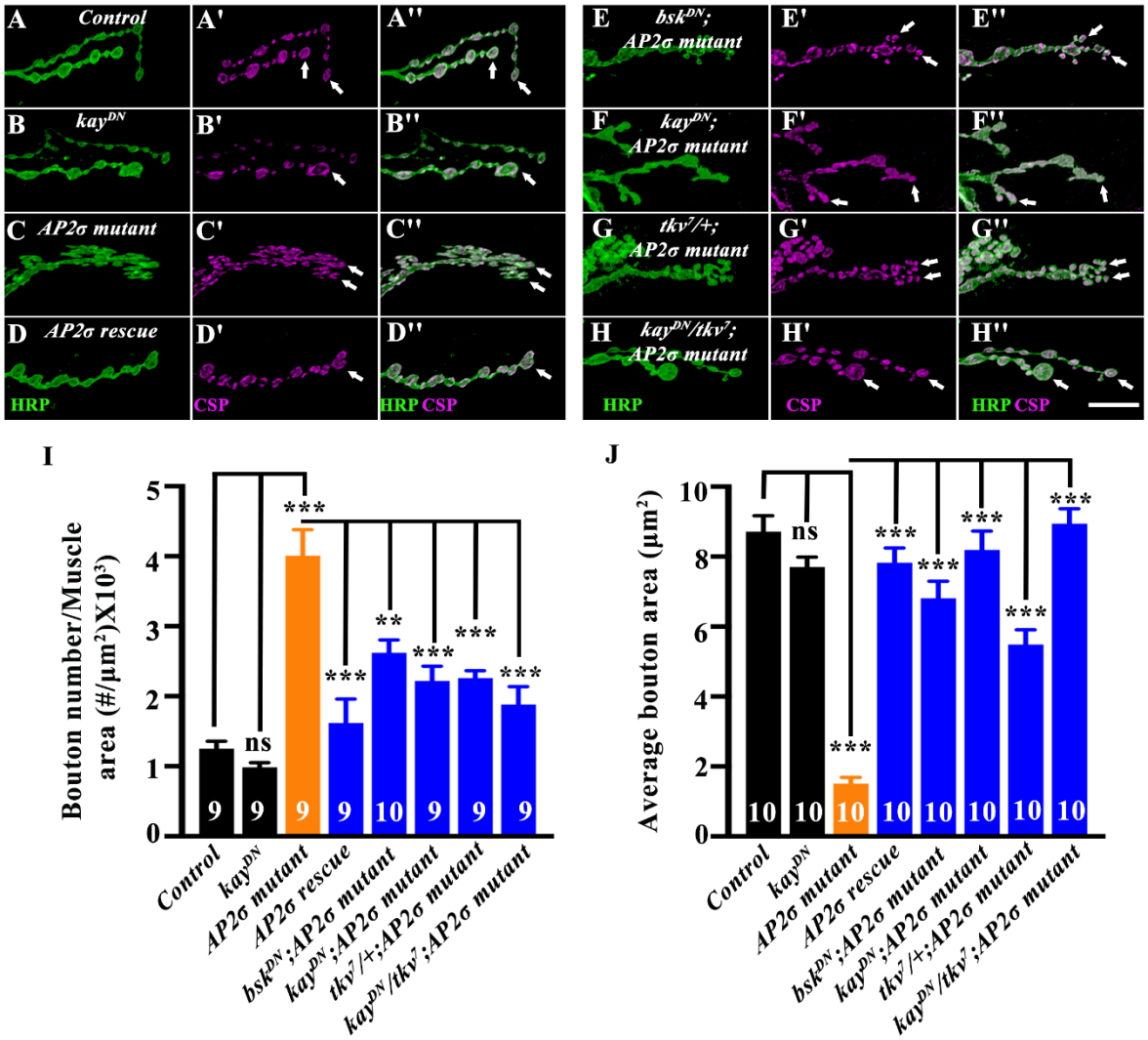
A Control
A'
A''
B kayDN
B'
B''
C AP2σ mutant
C'
C''
D AP2σ rescue
D'
D''
HRP
CSP
HRP CSP
E bskDN; AP2σ mutant
E'
E''
F kayDN; AP2σ mutant
F'
F''
G tkv7/+; AP2σ mutant
G'
G''
H kayDN/tkv7; AP2σ mutant
H'
H''
HRP
CSP
HRP CSP
I
Bouton number/Muscle area (#/μm²)X10³)
0
1
2
3
4
5
ns
***
**
9
9
9
9
10
9
9
9
Control
kayDN
AP2σ mutant
AP2σ rescue
bskDN;AP2σ mutant
kayDN;AP2σ mutant
tkv7/+;AP2σ mutant
kayDN/tkv7;AP2σ mutant
J
Average bouton area (μm²)
0
2
4
6
8
10
ns
***
10
10
10
10
10
10
10
10
Control
kayDN
AP2σ mutant
AP2σ rescue
bskDN;AP2σ mutant
kayDN;AP2σ mutant
tkv7/+;AP2σ mutant
kayDN/tkv7;AP2σ mutant

Figure_6

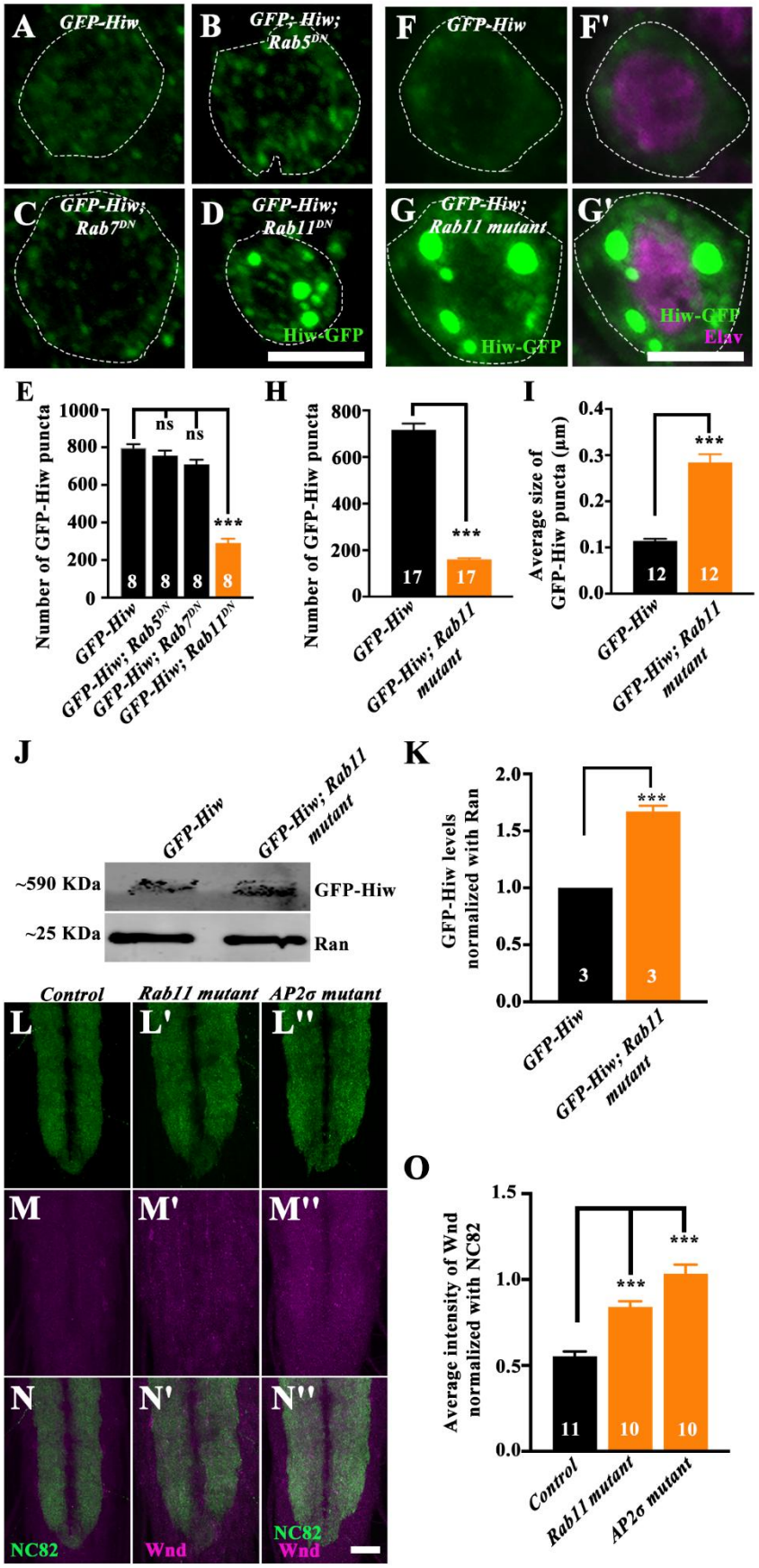
A
GFP-Hiw
B
GFP; Hiw; Rab5DN
F
GFP-Hiw
F'
C
GFP-Hiw; Rab7DN
D
GFP-Hiw; Rab11DN
Hiw-GFP
G
GFP-Hiw; Rab11 mutant
Hiw-GFP
G'
Hiw-GFP
Elav
E
Number of GFP-Hiw puncta
1000
800
600
400
200
0
ns
ns
***
8
8
8
8
GFP-Hiw
GFP-Hiw; Rab5DN
GFP-Hiw; Rab7DN
GFP-Hiw; Rab11DN
H
Number of GFP-Hiw puncta
800
600
400
200
0
***
17
17
GFP-Hiw
GFP-Hiw; Rab11 mutant
I
Average size of GFP-Hiw puncta (μm)
0.4
0.3
0.2
0.1
0.0
***
12
12
GFP-Hiw
GFP-Hiw; Rab11 mutant
J
GFP-Hiw
GFP-Hiw; Rab11 mutant
~590 KDa
GFP-Hiw
~25 KDa
Ran
K
GFP-Hiw levels normalized with Ran
2.0
1.5
1.0
0.5
0.0
***
3
3
GFP-Hiw
GFP-Hiw; Rab11 mutant
Control
Rab11 mutant
AP2σ mutant
L
L'
L''
M
M'
M''
N
N'
N''
NC82
Wnd
NC82
Wnd
O
Average intensity of Wnd normalized with NC82
1.5
1.0
0.5
0.0
***
***
11
10
10
Control
Rab11 mutant
AP2σ mutant

Figure_7

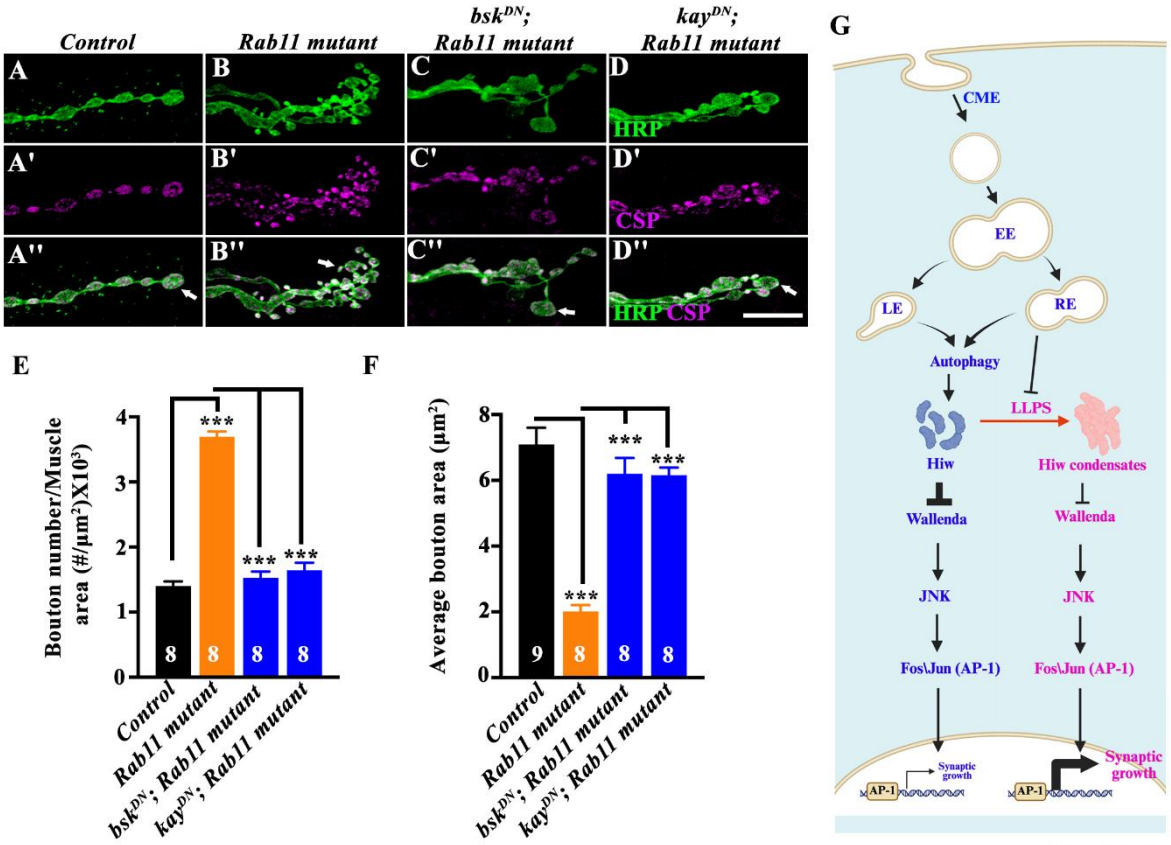
Control
Rab11 mutant
bskDN; Rab11 mutant
kayDN; Rab11 mutant
A
B
C
D
HRP
A'
B'
C'
D'
CSP
A''
B''
C''
D''
HRP CSP
E
Bouton number/Muscle area (#/μm²)X10³)
F
Average bouton area (μm²)
Control
Rab11 mutant
bskDN; Rab11 mutant
kayDN; Rab11 mutant
G
CME
EE
LE
RE
Autophagy
LLPS
Hiw
Hiw condensates
Wallenda
JNK
Fos\Jun (AP-1)
Synaptic growth
AP-1

Figure_8